Exploring Integrated Measurements in Autonomously Assembled Digital Material Systems

Derin Ulcay

Delft University of Technology

TU Delft

Exploring Integrated Measurements in Autonomously Assembled Digital Material Systems

by

Derin Ulcay

to obtain the degree of Master of Science
at the Delft University of Technology,
to be defended publicly on Friday April 25, 2025 at 14:00.

Thesis committee:

Chair	Prof. Clemens Dransfeld	TU Delft
Examiner	Dr. Otto Bergsma	TU Delft
Supervisor	Dr. Kunal Masania	TU Delft
Additional	Alex Luijten	TU Delft
Place	Faculty of Aerospace Engineering,	TU Delft
Project Duration	March 2024 – March 2025	
Student Number	4562836	

TU Delft


TU Delft
Delft
University of
Technology

Preface

Through my engineering education, I have come to appreciate the endless ways in which engineers redefine seemingly unsolvable real life problems to solve them in the abstract realms of mathematics and physics and work to bring their solutions back into the real world. While sometimes these methods involve simplifying and modelling the problem, a significant portion of them exploit transformations that render the problem easier to solve in a different context. The academic and extracurricular projects I have been a part of in the past couple of years have taught me a lot about myself and how much I enjoy exploring design concepts and embodiments that could help advance the state-of-the-art in unforeseen ways.

I am forever grateful to Professor Kunal Masania for allowing me to pursue a master's thesis project on doing just that: exploring the feasibility of transforming endemic assembly robots into measurement devices which feed information back into the system, closing the control loop. I thank Guillermo Presa for his work on designing the robot and the structure. I also thank PhD candidate Alex Luijten for guiding me during the last couple of months of my thesis project. Special thanks to Satya K. Ammu and many other Shaping Matter Lab members for making me feel part of the group during my stay.

Derin Ulcay
Delft, 6 November 2024


TU Delft
Delft
University of
Technology

Abstract

By breaking structures down into self-similar building blocks, digital manufacturing methods have come into the spotlight as a part of additive manufacturing. Progress in additive manufacturing has facilitated the production of more complex geometries and reduced material waste in the process. With the goal of scaling additive manufacturing up to the meso and macro scales, robotic assembly of cellular structures is increasingly being researched as a method to construct reconfigurable digital metamaterial structures. However, during robotic assembly and after the manufacturing is complete, the structural systems rely exclusively on external inputs if at all to estimate and monitor structural state. This thesis shows that the endemic robots used to manufacture the structure can also be used to measure deformations. The theoretical measurement characteristics of a bipedal inchworm robot have been calculated showing the expected resolution, accuracy, precision and dynamic range of measurements. Experiments have been conducted to construct a statistical measurement model and assess the nonlinearity of the measurement system. For a beam made up of 3D printed PLA cells with a relative density (p*/p) of 0.05, the results show that the robotic measurement system has resolution several times finer than the elastic range of bending and shear mode deformations for a beam with a single lattice cell cross-section. The robot can also detect stretch mode deformations on single lattice cross-section beams before structural failure. The thesis results demonstrate how inchworm locomoting bipedal assembly robots can be used to measure and monitor various deformations of slender lattice beams up to 3x3 cell cross-section, relying solely on the joint angle measurements used to control the robot. We anticipate this thesis to be a starting point for the integration of structural state measurements to the additive manufacturing process of robotic lattice cell assembly.


TU Delft
Delft
University of
Technology

List of Figures

List of Tables

List of Abbreviations

AM	Additive Manufacturing
BC	Boundary Condition
BS	Base Switched
CAD	Computer Aided Design
CFRP	Carbon Fibre Reinforced Polymer
CPP	Coverage Path Planning
DH	Denavit-Hartenberg
FFF	Fused Filament Fabrication
ILLA	Inchworm Locomoting Lattice Assembler
PM	Pre-Moved
SHM	Structrual Health Monitoring

Contents

1 Introduction

1.1 Motivation

In his book titled “Structures: or why things don’t fall down” Gordon defines a structure as “any assemblage of materials which is intended to sustain loads” [1]. Since the creation of the first tools, structures have supported and sheltered humankind paving the way to civilization. With advancements in technology, the structures engineered have also advanced, becoming more and more sophisticated. Consider for example the wheel, initially made from solid pieces of stone the structure has evolved over the years to become lighter with the inclusion of spokes and later came to be multi material partly inflated structures with the invention of pneumatic tyres.

Now in the digital age, manufacturing and knowledge of materials has enabled us to take another leap. By dividing and discretizing structures into self-similar units, digital manufacturing methods redefine structures as a collection of building blocks, similar to how digital computers have redefined images to be a collection of pixels. This representation has given birth to an approach to manufacturing where manufacturing is viewed as the process of additive assembly also known as additive manufacturing. Progress in additive manufacturing has facilitated the production of more complex structures and reduced material waste in the process.

The numerous achievements of additive manufacturing methods in micro scale manufacturing have invigorated research of additive manufacturing at the meso scale. One of the additive manufacturing methods being researched is the robotic assembly of cellular structures. While some researchers have built traditional gantry systems similar to those found in fused deposition manufacturing, Jenett, taking inspiration from manufacturing in biological systems, designed an assembly system using assemblers smaller than the size of the structure with inchworm robots; with this not only would the size of the structure not be limited by the manufacturing device but the manufacturing speed could also potentially be increased by parallelizing the assembly with many assembly robots [2].

Taking inspiration from Jenett, Luijten at ETH Zurich designed a similar robotic assembly system [3]. Later, Presa set to improve the system at TU Delft, enabling the construction of structures which do not conform to a grid [4]. This work proposes yet another improvement to the system: the use of the same inchworm locomoting robots that assemble the structure as measurement devices, during and after manufacturing, to feed information about the structural state back into the manufacturing system, closing the manufacturing loop. It is hoped that granting the structural system some awareness of its deformation state through robotic measurements, this work will contribute to the future implementation of a more reliable and self-aware living structural system.

Research into closing the manufacturing loop could usher many prospective avenues of research. Information on the deformation of the structure could guide the assembly order by indicating which locations need reinforcements. Deformation data could also allow the detection of faulty or failed cells during the assembly stage. It could also allow correcting of movement commands in slender overhanging structures. Finally, it could also open the door to assembly strategies involving robot actuated slender structures.

This research project is intended to form the basis of the classification and characterisation of the inchworm locomoting lattice assembler (ILLA) robot as a measurement device. Once the robot characteristics have been discovered, they can be used to assess the suitability of the ILLA robot for a given structural system or to find the limit bounds of lattice properties the structure must have to remain measurable with the robot.

1.2 Thesis Outline

This thesis is divided into three parts. Part I provides the background that lays the foundation to the rest of the thesis, Part II details the design improvements made and the experiments conducted, Part III concludes the thesis by reflecting on findings and suggesting future avenues of research.

Part I provides background information. It consists of chapter 2 which reviews the related literature, chapter 4 which provides theoretical background to the models used, and chapter 3 which defines the project scope & research questions. The literature review consists of the Gibson-Ashby theory developed to determine the properties of cellular materials, a review of engineered cellular materials, an introduction to digital material systems currently being researched, as well as characteristics of measurement systems, examples of robotic monitoring of structures and an introduction to the inchworm locomoting lattice assembler v3 (ILLAv3) robot and elastic joints. The theoretical background chapter briefly introduces Euler-Bernoulli beam theory and its assumptions, and then discusses the solutions derived for a concentrated force acting downwards on a cantilever beam. Then the equivalent stiffness, elastic modulus, and moment of area concepts are introduced in more depth. The research scope and definition chapter introduces the project scope by classifying activities into four quadrants and providing an overview of activities that fall into each quadrant. It then describes the aims of the project and ends with the introduction of research questions to which this thesis project aims to answer.

Part II deals with the design, methodology and results. The first chapter in Part II begins with an account of preliminary experiments conducted to assess feasibility, it then features the improvements made to the hardware platform which directly influence the performance of the robot both as a measurement device and as an assembler. The second chapter begins with an analysis of the ILLAv3 robot and the robot+lattice structural system. The section then introduces the statistical tip deflection and load estimation model and calculates the theoretical characteristics of estimator candidates. The next section goes over the experimental plan and schedule for the experiments used to construct the statistical model. The following section describes the observations made during the course of experiments and exposes insights about the system not covered in the theoretical model. Lastly, the results and discussion sections summarize the results of experiments, discuss the applicability of the results, reflect on the results & chosen methodology, and give recommendations on robot pose choice.

Finally, Part III provides a conclusion to the thesis answering the research questions and further summarizing key results. The final chapter describes the context of the project, discusses the significance of integrated measurements, and explores future avenues for robotic measurement systems.

Part I

Background


TU Delft
Delft
University of
Technology

2

Literature Review

2.1 Cellular Solids

Many materials have a repeating underlying microstructure comprised of cells with surface or edge features. Examples in nature include honeycombs which partition the beehive wall into hexagonal cells with minimal material used and sea sponges which use their porous structure to ingest food and oxygen with the flow of water. Taking inspiration from nature, engineers have produced cellular solids to exploit a large variety of properties. Currently, hexagonal honeycomb cores are now commonly found in sandwich panel designs to enable lightweight yet stiff planes. Similar to sponges, open-cell metallic foams have found use in heat exchange devices to transfer heat to fluids. Many other examples exist, such as cellular foams which allow large deformations at constant load, which are used commonly from cushioning applications to impact absorption devices such as helmets; or closed-cell foams with gases trapped inside, which found use in thermal insulation [5].

Cellular solids are typically categorized into two primary types based on their internal architecture: open-cell and closed-cell structures. Open-cell materials have interconnected pores or voids. Closed-cell materials, by contrast, feature volumes enclosed by surfaces as Figure 2.1 shows.

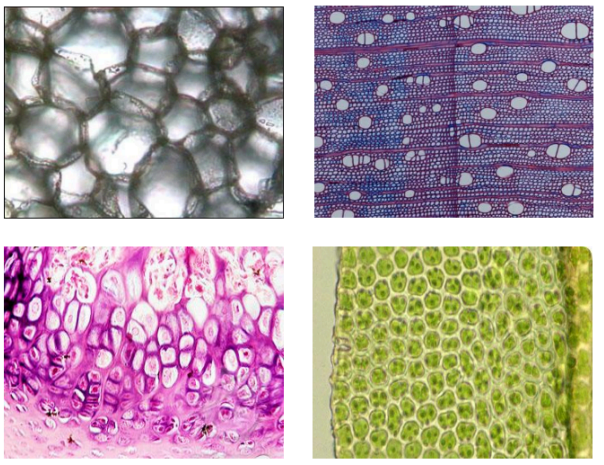

(a) Closed-cell materials. (top left) cork, (top right) wood, (bottom right) leaf; and hybrid cellular material (bottom left) bone.

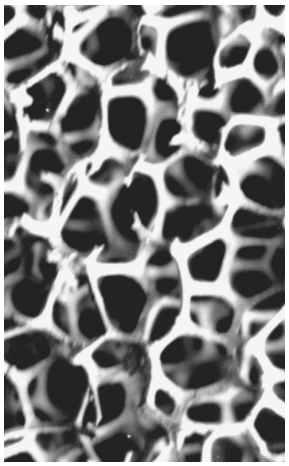

(b) Typical open-cell material.

Figure 2.1: Examples of closed-cell and open-cell cellular materials. Images reprinted from [6] and [7] respectively.

Depending on the topology, cellular structures either deform by bending of the cell walls/struts or by stretching and compressing of the wall elements. Bending cell structures are particularly useful for their compressive load saturation: the structure undergoes deformation under a constant load after buckling of the walls/struts. Stretch dominated structures on the other hand have high mechanical efficiency [5, 7].

The deformation behaviour (buckling or stretch dominated) of a structure are deduced from the Maxwell stability criterion in three dimension:

$$M = b - 3j + 6 = s - m, \tag{2.1}$$

where b is the number of struts, j is the number of joints. s is the number of self-stress states and m is the number of mechanism states [7].

$$\begin{aligned} M \leq 0 \implies & \text{the structure is a mechanism,} \\ & \text{free to move in unsupported directions,} \\ & \text{as demonstrated in Figure 2.2 a.} \\ M = 0 \implies & \text{the structure is statically determinate,} \\ & \text{stretch dominated behaviour,} \\ & \text{as demonstrated in Figure 2.2 b.} \\ M \geq 0 \implies & \text{the structure is overconstrained,} \\ & \text{internal stresses may be present} \\ & \text{even in the absence of external loads,} \\ & \text{as demonstrated in Figure 2.2 c.} \end{aligned} \tag{2.2}$$

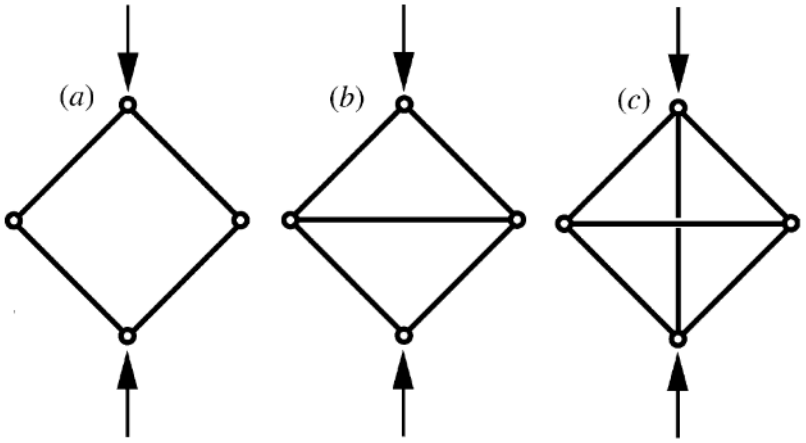

Figure 2.2: Two-dimensional structures of different Maxwell mechanical states. Figure reproduced from [7].

The mechanical properties of cellular solids are calculated by using the Gibson-Ashby model. The Gibson-Ashby model relates the mechanical properties to the relative density of the cellular solid [8]:

$$\begin{aligned} E^* &= E_s \cdot C \cdot \left(\frac{\rho^*}{\rho_s}\right)^n \\ \sigma_y^* &= \sigma_{y_s} \cdot C' \cdot \left(\frac{\rho^*}{\rho_s}\right)^m \end{aligned} \tag{2.3}$$

Where the properties with an asterisk are the E-modulus and yield strength that belong to the cellular solid, the properties with subscript s belong to the base material; C, C', m and n are experimentally determined constants dependent on the type of deformation the lattice undergoes and the cell topology.

2.2 Engineered Metamaterials

The emergence of lattice structures represents a more advanced and specialized subset of cellular solids: engineered metamaterials. Historically, the use of lattice structures was limited by manufacturing capabilities, but the development of additive manufacturing (AM), particularly 3D printing, has made it possible to fabricate these intricate designs [5]. Unlike foams, which often exhibit a random distribution of voids, lattice structures usually consist of highly regular and periodic arrays of beams or struts. These geometrically controlled architectures could be designed to optimize specific material properties. Compared to traditional materials these architected metamaterials offer advantages particularly in their ability to achieve a high strength-to-weight ratio, a property that is critical in aerospace applications. An example is the material designed by Cheung (Figure 2.3) boasting a stiffness of 12.3 megapascals at a density of 7.2 milligrams per cubic centimeter [9].

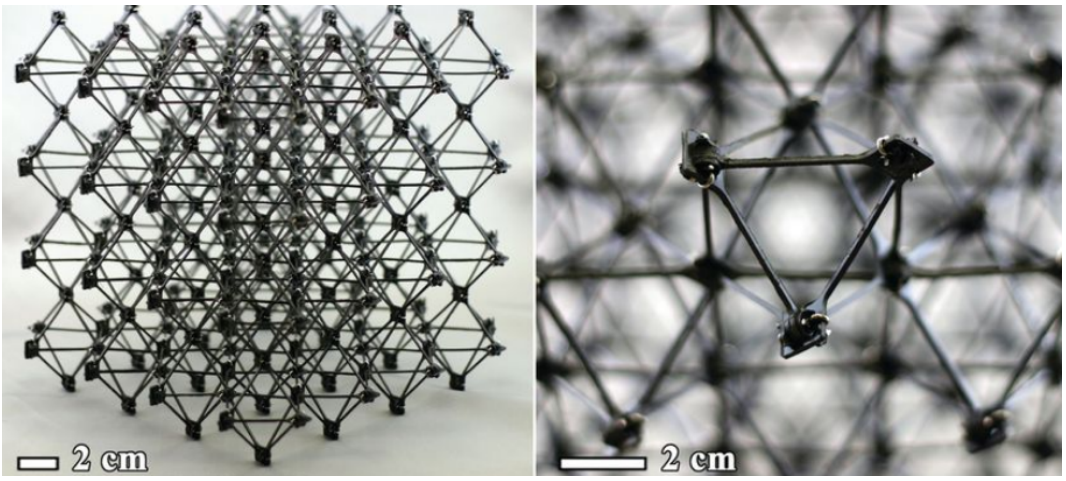

Figure 2.3: Reversibly assembled engineered metamaterial comprised of a repeated octahedral cell pattern; view of the structure on the left and the octahedral cell on the right. Image reprinted from [9].

The design space for architected metamaterials are obtained and visualized by using an Ashby chart. In Figure 2.4, from the base material property ”A” (carbon fibre reinforced polymer (CFRP) in this case) two bounding lines for stretch dominated cellular structures (represented with the higher dashed line) and bending dominated cellular structures (represented with the lower dashed line) are projected. The relative density chosen for the cellular solid determines where along the line the elastic modulus and bulk density of the material will be, as the 3 examples in ”C” shows. In reality, the behavior of the cell will exhibit properties between the purely stretch dominated line and purely bending dominated line as ”B” shows, and the resulting property will be somewhere in the bounded area as ”D” shows.

Additionally, by tailoring the unit cell geometry of the lattice, the stiffness and mass distribution can be optimized to create materials with desired natural frequencies. These lattice structures can then act as mechanical filters, isolating particular frequency bands and preventing those vibrations from propagating through a structure [11]. Another use in energy harvesting applications: the material response can be tuned to match the environment, allowing a piezoelectric material to ingest and convert a larger amount of energy from surroundings [12].

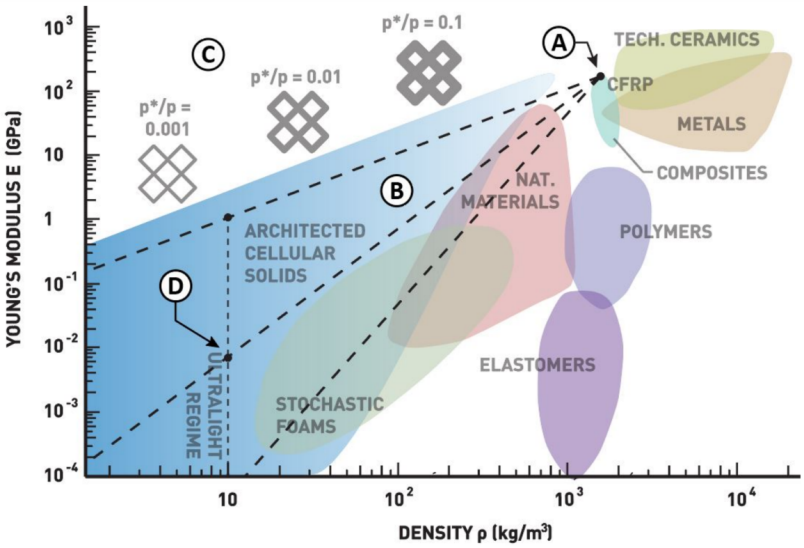

Figure 2.4: Properties of architected cellular solids made from CFRP. Figure reprinted from [10].

2.3 Digital Material Systems

Digital materials are materials build from modular building blocks that share an interfacing pattern, similar to LEGO bricks. Unlike traditional manufacturing techniques, which rely on continuous materials shaped through cutting, molding, or casting, digital materials are composed of discrete, modular components. These ”building blocks” are combined using their self aligning and interlocking geometry to form structural systems. The placement freedom and composability of the structure allows the structural system great adaptability to many applications. Much like bits in computing, simple blocks may be combined and configure to create complex functional systems. With a set of building blocks with diverse properties, the properties of a structure could be ”programmed” into the assembly of individual parts, each contributing specific mechanical, electrical, or thermal characteristics.

One of the most studied digital material systems are enzymes: composed from the 22 α-amino acid building blocks, these polypeptide chains form 3-dimensional structures which drive all the metabolic chemical processes we call life [13]. In the late 20th century, Toffoli and Margolus worked on programmable matter as a means to more efficient computation [14]. In the same period the work of Lehn started the field of supramolecular chemistry, studying how molecules embody and recognize information [15]. Lehn's work led to the birth of fields such as nanofabrication and microrobotics. In 1998, Murata et al. proposed and showed a 3-dimensional self-reconfigurable structure in which the blocks communicated with neighbouring blocks to form a distributed intelligence structural system [16]. Later many implementations of intelligent robot structures were researched such as the self-assembling and self-repairing structural organism by Levi et al. [17]. Some images of these are shown in Figure 2.5.

Looking at ways to scale the self-assembly and manufacturing of structures to digital structures of tens of thousands of blocks, Jenett et al. devised a material robot system consisting of cuboctahedral cells called voxels and two types of relative robots (BILL-E and MOJO) to carry the cells and assemble them [2, 19].Building on top of this work, Abdel-Rahman et al. designed self replicating multi-scale assembly robots made from the cuboctahedral cells they carry [20]. Taking inspiration from the material-robot separation in the work of Jenett et al., NASA and Luijten has designed a similar system consisting of cuboctahedral and octahedral blocks respectively [3]. Bironi then designed a cuboctahedral lattice for robotic assembly which reduced system complexity and assembly time. Continuing on

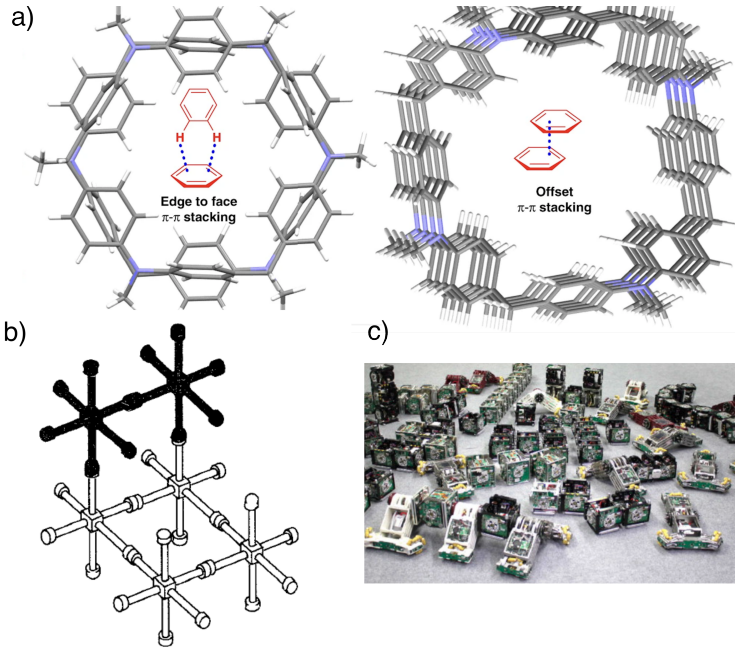

Figure 2.5: Digital material research. (a) Edge and face stacked diphenylamine[n]arene structures result of supramolecular chemistry n=3&4, (b) Self-reconfigurable structure, (c) Reconfigurable structural organisms. From [18], [16], [17] respectively.

their work, Presa Magriñá at the Shaping Matter Lab at TU Delft designed a new version of the structural system [4]. Images of material-robot structural systems are shown in Figure 2.6. Currently, Abdel-Rahman and Gershenfeld et al at the Bits and Atoms lab at MIT are researching the self replication aspect of assemblers [21]. Cheung et al at NASA are working on realising modular cuboctahedral structural systems for space infrastructure [22]. Masania, Luijten and Nettersheim of the Shaping Matter Lab are researching the manufacturing of structural systems with robotic assemblers and engineered living material cell blocks [23].

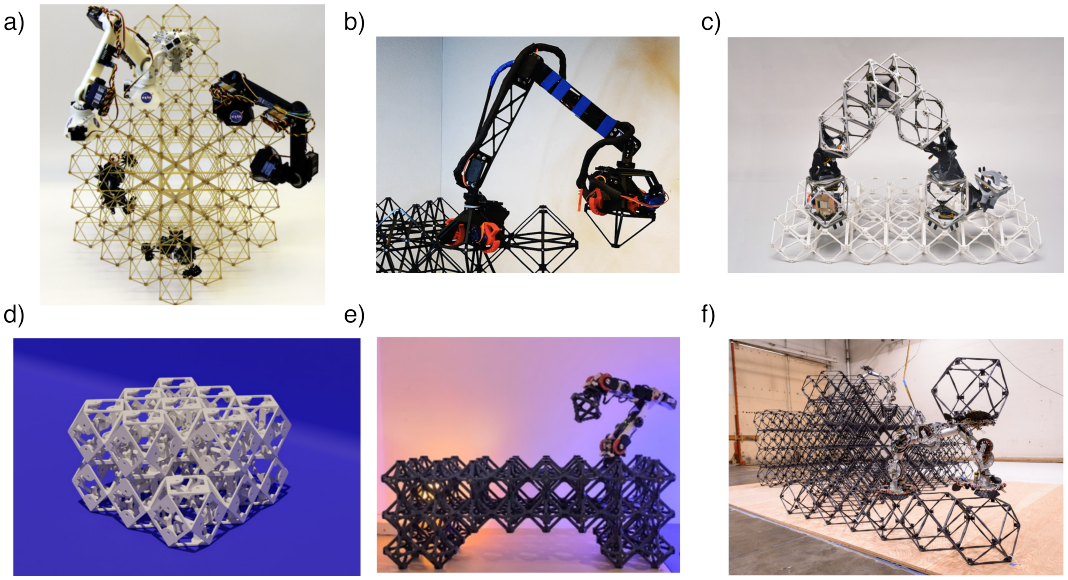

Figure 2.6: Material-robot systems. (a) BILL-E 1.0 and MOJO robots with octahedral cells, (b) Luijten's relative robot with octahedral cells, (c) MIT self-replicating robot with cuboctahedron cells, (d) Bironts cuboctahedral lattices, (e) the ILLA robot with octahedral cells, (f) NASA's SOLL-E with cuboctahedral cells. Images reprinted from [24], [3], [20], [25], [4], [26] respectively.

The concept of programmable, modular materials could enable rapid construction and reconfiguration of buildings in response to changing environmental or societal needs. They could also make structures in remote environments such as orbits in space more easily repairable through their modularity. Digital materials also offer the possibility of circular material use—since the components are discrete and modular, they can be easily recycled, repaired, or re-used, aligning with the goals of sustainable design and manufacturing.

2.4 Characteristics of Measurement Systems

Anisimov, Groves and Schoemaker describe structural measurements as the act of gathering quantitative information about a structure's state. The usefulness of the information obtained is judged on three aspects [27]:

- Descriptiveness: clear relationship between measurements and state variables
- Selectiveness: irrelevant variables are not measured
- Objectivity: the independence of the measurement to the operator and ideally also environmental conditions

In characterizing a measurement system, the primary parameters that define the behavior and limitations of a measurement system are sensitivity, resolution, accuracy, precision, hysteresis, stability, and dynamic range [27, 28].

Sensitivity refers to the ratio of the change in the output signal to the change in the input signal. It defines the system's ability to respond to small changes in the quantity being measured.

Resolution is the smallest detectable change in a quantity that the system can register. It is typically determined by the inherent noise and sensitivity of the measurement device. Systems with higher resolution can discern finer variations in the measured signal.

Accuracy is the degree of conformity of a measured quantity to its true value. It represents the combined effect of all systematic errors in the measurement process. Accuracy is determined by calibration against a known standard and is expressed as the difference between the true value and the measured value, often given as a percentage of the true value.

Precision reflects the consistency of measurements under the same conditions. It is quantified by the standard deviation of repeated measurements, representing the random errors or noise in the system. Precision does not address the proximity of the measurements to the true value, but the system's ability to produce similar results upon repetition.

Hysteresis, also known as a memory effect is the dependence of a measured quantity on prior states.

Stability describes a system's ability to maintain consistent performance over time. Long-term stability, often referred to as drift, is the degree to which a system's output changes over time without changes in the input signal. Creep/relaxation of the measurement device is a form of instability.

Range describes the highest and lowest quantities that can be measured by a measurement system. For some measurement systems it is provided as a ratio of highest quantity over lowest quantity, sometimes in a logarithmic scale (in decibels) and is named dynamic range.

2.5 Perspectives on the Robotic Monitoring of Structures

2.5.1 Observability of Dynamic Systems

Kalman, in 1960 in developing the theory of control systems introduced the concepts of observability and controllability of a plant [29]. In their work, Kalman studies the intrinsic characterization of plants (systems) constrained at the output. For such a plant, a costate $z*$ of a plant is a state within the space of linear functions of state variables X. $z*$ is said to be observable if its value can be determined from measurements of the output signal within a bound timeframe.

Traditionally, the system boundaries of a robot from a control system point of view are limited to the links and joints of the robot. Encoders, visual sensors, force sensors are used in different types of robots to make the system fully observable for this scope. Changing the system boundaries to cover the whole or a local portion of the structure and investigating which expanded system states (now including structural states) the robot outputs can still observe is one way of formulating the research question for this thesis. A similar approach has been demonstrated for a gripper-climber robot and bamboo construction system using optical camera sensors and magnetic encoder data along with machine learning algorithms to drive the robot control behaviour in manipulating bamboo bundles [30].

2.5.2 Structural Health Monitoring Definition

Groves, citing Boller's definition in the Encyclopedia of Structural Health Monitoring (2014) defines structural health monitoring (SHM) as the incorporation of sensing and actuation into the structural system in a non-destructive way to allow the loading and/or damage conditions to be recorded [31].

Groves proceeds to divide SHM functionalities into levels:

- SHM Level 1: Online Load Monitoring

  Determination of whether loads are within operational limits and potential quantification of loads and environmental conditions. The undertaken thesis aims to achieve monitoring at this level.

- SHM Level 2: Detection and Localization of Damage
- SHM Level 3: Quantification of Size and Type of Damage
- SHM Level 4: Prediction of the Remaining Life of the Structure

2.5.3 Examples of Robotic Monitoring

The use of robots to observe and inspect structures especially in dangerous environments is a topic gathering a lot of interest.

Almadhoun et al has surveyed robotic inspectors with an emphasis on comparing coverage path planning (CPP) algorithms which allow the full structure to be reconstructed as a model [32]. The model based path planning approaches presented both in terms path generation algorithms and in terms of evaluation metrics and methods provide valuable examples of how a mobile robotic measurement device could be used to provide a complete picture of the structure.

Tian et al surveyed both rigid and soft robots used for static and dynamic observations with a focus on monitoring structures and identifying multimodal robot use trends. 16 robots are compared [33]. The study is particularly interesting for including SHM 1 level observation robots for also dynamic conditions alongside damage detection robots more commonly found in other studies.

Manh La et al has designed an image based surface level defect inspecting robot for application in steel bridge structures [34].

Jhanshahi et al has reviewed uses of robot swarms as measurement networks for in-situ active sensing. The paper compares 10 modular robot systems [35]. This paper presents an alternative to single robot path coverage based approaches with a swarm network to collect structural state data in a more distributed way.

Majority of the studies indicate that the major challenges lie in adapting to the different features present in structures currently used, localization of the robot and mapping of the structure, and finally accuracy of measurements. For digital cellular structures, the number of structural features are drastically simpler. Furthermore, localization of the robot and mapping of the structure is also an easier problem due to the discrete nature of the traversal problem already solved by Presa Magriñá [4]. This leaves the accuracy of measurements as the ultimate concern for the digital structural systems.

2.6 Robot Mechanical Design and Repeatability of Movement

2.6.1 ILLA v3

The ILLA v3 is the bipedal inchworm locomoting robot designed by Presa Magriñá during his master thesis [4].

The robot features 3 joint locations, the first and last being differential cable driven joints with two smart servos each, while the middle joint is a single degree of freedom joint directly driven by a single servo. All 5 servos are equipped with an absolute magnetic rotary encoder featuring a resolution of 0.1 degrees and an accuracy of 0.2 degrees[1].

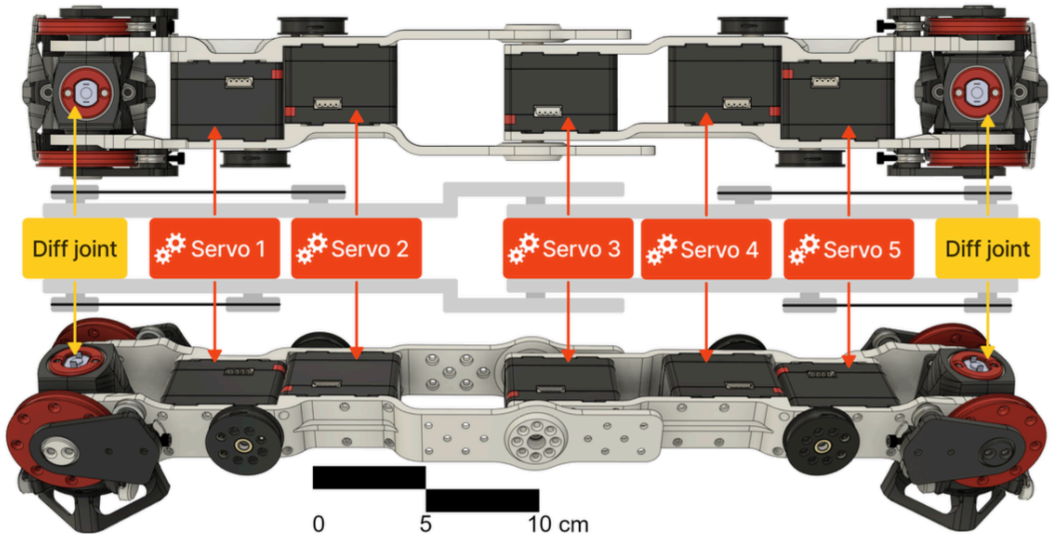

Figure 2.7: The computer aided design model of the ILLA v3 robot. Reprinted from [4].

The robot completed the pick and place task for a single octahedral lattice cell in early 2024 with some adjustments. Namely, the joint 3 commands were given with a reference offset of 1 degree to compensate for backlash. The screw in operation was adjusted with some jiggle motion and the rotation was repeated back and forth 6 times

[1] https://wiki.lynxmotion.com/info/wiki/lynxmotion/view/ses-v2/lynxmotion-smart-servo/lss-specifications/

While the directly driven joint is common, the space constraints at the gripper joint locations have lead to a cable-driven differential joint design similar to that found in the exoskeletal elbow joint designed by Chen et al. [36].

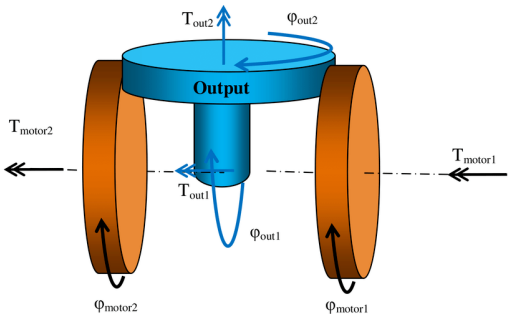

Figure 2.8: Illustration showing the working principle of differential joints. Reprinted from [37].

The differential joint combines the inputs of two servos to rotate the joint about two axes. Figure 2.8 shows how two servos (orange) can actuate the joint (blue) both around the servo pulley axis (ϕ_{out1}) and around the output symmetry axis (ϕ_{out2}) by rotating the servos in opposite or similar directions. Figure 2.7 shows servos 1-2 and 4-5 which actuate the left and right differential joints with cables. The cables are attached to the servos via the black pulleys and fixed at this location with a screw. The cables then pass through a cable tensioner mechanism which aims to remove the slack in the cables. It goes through the red pulleys and is attached at the grippers.

Cable driven designs are commonly find in biologically inspired bipedal walking robots such as the Spring Turkey and Spring Flamingo robots [38, 39]. Similar to the elbow previously mentioned the author of these robots make use of an approach named series elastic actuators which is a joint design approach straying from the traditional. In their words ”It is traditional to make the interface between an actuator and its load as stiff as possible. Despite this tradition, reducing interface stiffness offers a number of advantages, including greater shock tolerance, lower reflected inertia, more accurate and stable force control, less inadvertent damage to the environment, and the capacity for energy storage. As a trade-off, reducing interface stiffness also lowers zero motion force bandwidth.” [40]. In all cases the driving cables act as elastic elements between the servos and the joints being actuated. The quote from Pratt et al, already explains the advantages relating to shock tolerance and inertia however the capacity of energy storage of the elastic elements mentioned contribute to hysteresis in joint movements and measurements [41]. Additionally, Hwangbo et al in their work presenting a cable driven jumping robot Capler-leg, as well as most of the above-mentioned robots feature groove features on their pulleys to ensure the cable lengths remain the same. This feature is missing in the ILLA v3 [42]. Cable driven designs bring about an additional tradeoff: while tensioning the cables helps reduce backlash the higher tension increases the friction at the joints. Finally, It is also worth mentioning that cable driven system unlike infinitely rotating gear systems have a limited range of movement.

Regardless of the drive solution chosen for the robot design; the ideal characteristics of measurement systems (repeatability, resolution, accuracy, hysteresis, and stability) align very closely with the performance characteristics expected for the control of the robot. This in turn means that improvements to the robot are likely to benefit both the control characteristics and the measurement capabilities of the robot.


TU Delft
Delft
University of
Technology

3

Research Scope and Definition

3.1 Thesis Project Scope

The current implementation of inchworm robot material systems rely exclusively on the state of the ideal state of the structure for manufacturing. This makes the process prone to failure in the presence of disturbances. This thesis aims to explore inchworm robot contact measurements as a way of introducing more awareness of structure state to robotic manufacturing system. Feeding this information back could allow the manufacturing system to respond to and strategise for both predictable and unpredictable factors external to the digital representation of the structure, paving the way for robust data driven manufacturing and maintenance processes. This project takes the first steps in exploring robotic contact based measurements experimentally and theoretically to discern the measurement capability and characteristics of the ILLA robot.

The activities of this thesis can be broadly divided into three:

Testing

A cantilever beam setup is used to determine the robot measurement ability at various robot poses, positions, and preconditions. The theory, results and limitations are discussed in chapter 6. Experiments are scoped to only include tests of bending mode deformations as this was identified as the most pliable mode and poses the greatest threat to assembly during manufacturing.

Hardware Development

Firstly, the partly dysfunctional ”main” printed electronic circuit board (PCB) was re-designed with different components and layout changes. Secondly, the tensioner system for tensioning the cables which drive the differential joint has also been re-designed to provide adequate tensioning performance for more responsive differential joints, more durability increasing longevity and reliability, and more range helping the assembly process. Finally, the gripper has been changed to closely matched the updated lattice geometry and provide a firmer fit, helping both the self alignment during docking and conformation once docked. The details are presented in Appendix C (PCB) and in chapter 5 (tensioner and gripper).

Estimation of deformations

A single mode statistical model of the beam structure given robot angle measurements has been created by using the magnitude of the base to end distance calculated from servo angle measurements. Though more work is required to make it a complete implementation (currently limited to single mode at a time, tip deflection only), it serves as a digital summary of the results of the experiments and a very simple demonstration of how data driven approaches could be used in the future.

3.2 Research Questions

This thesis project aims to answer the following research questions:

- How can meso-scale digital structural systems be made self-aware, completing the structure – digital-twin information loop?
    1. What magnitude of deformation can be expected of such a two scale structure, how does it behave?
    2. To what extent can the ILLA robots reliably detect and measure these deformations?
    3. How can the deformation of the overall structure be estimated using a set of local, surface level measurements?

4

Theoretical Background

4.1 Euler-Bernoulli Beam Theory

A beam is a structure who has one dimension much larger than the other two. The axis of a beam is defined along the long dimension. Several solid mechanics theory of beams or beam theories have been developed over time to simplify the calculations of beam deflections under loading; each with its set of assumptions. One of the most widely used models is the one developed by Bernoulli and Euler called Euler-Bernoulli beam theory. The assumptions for this model are that plane sections remain plane, undeformed along the section plane, and perpendicular/normal to the deformed beam axis [43]. This leads to the following relationships to be formed:

$$EI\frac{d^4w(x)}{dx^4} = q(x), \tag{4.1}$$

where E is the elastic modulus, I is the area moment of inertia, $w(x)$ is the deflection of the beam at position x, and $q(x)$ is the distributed load acting on the beam.

The tip deflection of an Euler-Bernoulli beam subjected to a concentrated vertical force is then given by:

$$\delta_{\text{tip}} = \frac{Pa^2}{6EI}\left(3l - a\right), \tag{4.2}$$

where a is the location along the beam the concentrated force P acts on, l is the length of the beam, E is the elastic modulus of the beam material, and I is the second moment of area of the beam cross-section.

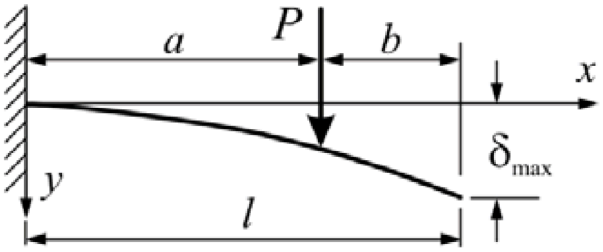

Figure 4.1: Illustration of an Euler-Bernoulli beam under a vertical load P.

The vertical displacement at any coordinate x along the beam is given by:

$$y = \begin{cases} \frac{Px^2}{6EI}\left(3a - x\right) & \text{for } 0 \leq x \leq a, \\ \frac{Pa^2}{6EI}\left(3x - a\right) & \text{for } a \leq x \leq l. \end{cases}$$

The rotation of the beam at any x coordinate along the beam is defined by:

$$\theta(x) = \begin{cases} \frac{Px}{2EI}\left(2a - x\right), & \text{for } 0 \leq x \leq a, \\ \frac{Pa^2}{2EI}, & \text{for } a \leq x \leq l. \end{cases}$$

4.2 Equivalent E-Modulus and Area Moment of Inertia of Discrete Lattice Beams

Using Gibson-Ashby theory, the equivalent stiffness of a stretch dominated cellular material can be approximated with the following relationship [7]:

$$\frac{\tilde{E}}{E_s} \approx \frac{1}{3}\frac{\tilde{\rho}}{\rho_s}, \tag{4.3}$$

where $\tilde{E}$ is the elastic modulus of the cellular material, E_s is the elastic modulus of the base material, $\tilde{\rho}$ is the density of the cellular material, and ρ_s is the density of the base material.

The lattices employed in this project have a relative density $\tilde{\rho}/\rho_s$ of 0.05. Given the flexural elastic modulus for a 3D printed PLA part of 3019 MPa in the relevant direction (provided by Ultimaker, a fused filament fabrication (FFF) material provider[1]) the equivalent cellular material elastic modulus can be calculated using Equation 4.3 to be 50.3 MPa.

However, Jenett has shown that for sparse cross-sections the lattices are underconstrained and the lattice connectivity is not sufficient to reach the continuum value. Figure 4.2 shows the behavior of underconstrained lattice beams in comparison to the continuum value calculated with the Gibson-Ashby theory. Assuming this model holds true also for octahedral lattice cells, we can calculate the expected modulus of 2x2 and 3x3 lattice cell cross-section beams relative to the 1x1 lattice beam. Table 4.1 presents the factors used to determine 2x2 and 3x3 beam section elastic moduli.

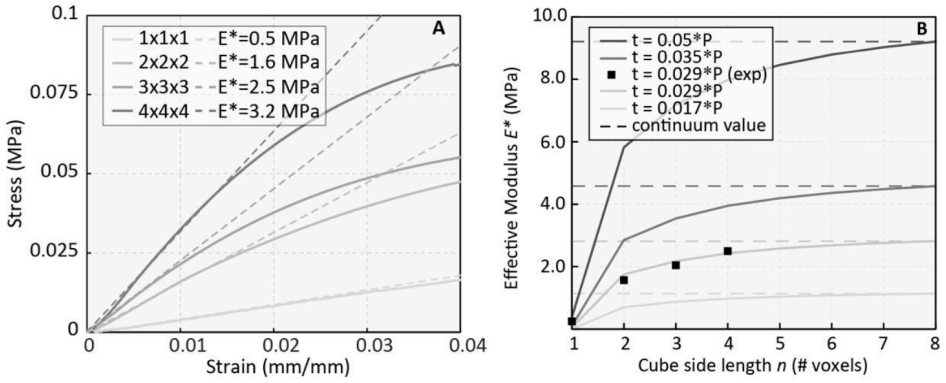

Figure 4.2: Lattice effective modulus and stress strain graphs for underconstrained lattice beams. Reprinted from [10].

There are two ways to approach the area moment of inertia of a sparse lattice beam. One way is to model it directly from the lattice geometry and the other way is to still assume a bulk cellular material taking the entire space the lattice occupies to calculate the area moment of inertia. The first approach gives more insight into the behaviour of sparse lattice beams since it does not assume a bulk material or the connectivity expectation. However,

[1] https://www.plgglobal.co.uk/wp-content/uploads/2022/07/Ultimaker-PLA-TDS-v5.00.pdf

Table 4.1: Summary of elastic moduli of different cross-section discrete lattice beams.

Beam Cross-section	Effective Modulus Factor
1x1	1/18
2x2	3.2/18
3x3	5/18

the second approach allows a more direct comparison with the expected bulk material properties, similar to Figure 4.2. For this analysis we have chosen to use the second option, but the first approach and the insights gained from it can be found on Appendix B. Since the cross-section geometry plays a large role in bending via the second moment of area I, modelling the lattice beam as a bulk material implies a large assumption.

The area moment of inertia of a square cross-section is given by:

$$I = \frac{a^4}{12}. \tag{4.4}$$

The area moment of inertia of a 100 mm x 100 mm square section is therefore $\frac{100^4}{12} mm^4$. Similarly, the area moment of inertia of larger cross-section beams can be calculated.

Table 4.2: Summary of lattice area moment of inertias for different cross-section discrete lattice beams.

Beam Cross-section	Second Moment of Area Factor
1x1	1
2x2	16
3x3	81

The beam bending stiffness (EI) of single lattice cross-section beams can be experimentally determined. The higher cross-section (2x2, 3x3) sparse beam moduli can then be calculated by using the effective modulus factors shown in Table 4.1 and the increased area moment of inertia documented in Table 4.2, as shown in Equation 4.5.

$$(EI)_{\text{beam}} = C_{\text{effective-modulus}} \cdot E_{\infty} \quad \cdot \quad C_{\text{moment-of-area}} \cdot I_{\text{1x1}}. \tag{4.5}$$

4.3 Forward Kinematics of Inchworm Lattice Assembler Robots

Forward kinematics is a fundamental concept in robotics that deals with determining the position and orientation of the joints and the end gripper based on the known joint angles of a robotic manipulator. It provides a direct mapping from the robot's joint space (angles) to its workspace (Cartesian coordinates).

The forward kinematics problem can be formulated as a sequence of transformation matrices:

$$\mathbf{T}_n = \mathbf{T}_1 \mathbf{T}_2 \cdots \mathbf{T}_n.$$

Where;

- $\mathbf{T}_i$ is the homogeneous transformation matrix for the i^{th} joint or link, encapsulating the rotation and translation due to that joint;
- $\mathbf{T}_n$ represents the overall transformation from the base to the n^{th} joint.

Each transformation matrix is derived by using the Denavit-Hartenberg (DH) convention, which simplifies the systematic derivation of these transformations by defining specific parameters:

- θ_i: Joint angle (for revolute joints),
- d_i: Joint offset (for prismatic joints),
- a_i: Link length,
- α_i: Link twist.

The resulting transformation matrix for a single joint is:

$$\mathbf{T}_i = \begin{bmatrix} \cos\theta_i & -\sin\theta_i \cos\alpha_i & \sin\theta_i \sin\alpha_i & a_i \cos\theta_i \\ \sin\theta_i & \cos\theta_i \cos\alpha_i & -\cos\theta_i \sin\alpha_i & a_i \sin\theta_i \\ 0 & \sin\alpha_i & \cos\alpha_i & d_i \\ 0 & 0 & 0 & 1 \end{bmatrix}$$

By multiplying these matrices sequentially, the transformation describing each joint location up to the end point (gripper) can be found.

The joint configuration of the ILLAv3 robot is described in Figure 4.3. Joint 0 is the base, joint 4 is the end gripper location, servo pairs 1,2 and 4,5 differentially drive the rotations of joints 1 and 3 respectively while servo 3 directly drives joint 2.

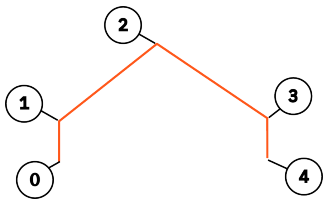

Figure 4.3: Illustration of the simplified ILLA robot showing the naming of each joint.

Part II

Design, Methodology & Results


TU Delft
Delft
University of
Technology

5

Preliminary Experiments and Contributions to the Hardware Platform

Preliminary experiments in the spirit of a proof of concept were planned and performed to assess whether the current material robot system was suitable for measurement use and to better understand how measurements would work in practice. The observations made helped define what is desired from an experimental setup, as well as which aspects of the robot design posed immediate challenges.

Several contributions were made to the ILLAv3 to amend and improve its design. Sections later in this chapter detail and provide reasoning for these changes.

5.1 Preliminary Exploratory Experiments

The setup consisted of a cantilever lattice beam screwed on to a heavy workshop table made of steel. Duct tape was fashioned into a belt like attachment piece and screwed onto the bottom of the furthest lattice. A luggage weight measurement device (with resolution of 0.1 kg) was used as a load cell hanging from the attachment piece. A 5 litre measurement jug was re-appropriated as a bowl with some electrical cable as a handle and hung from the load cell. Two 500 ml PET water bottles were filled with water until they had a mass of 500 g (measured with a balance to a 0.1 g precision) and used as weights to be placed in the bowl.

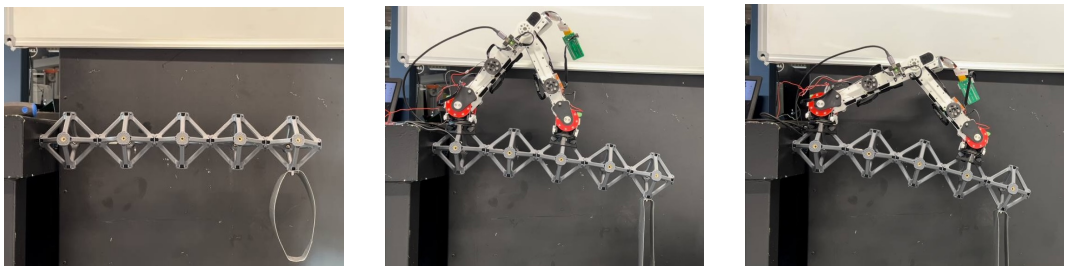

(a) The beam without the robot.

(b) 1 lattice apart pose, loaded with 500 mg mass.

(c) 2 lattices apart pose, loaded with 1000 mg mass.

Figure 5.1: Example images of the exploratory experiment setup.

The robot was placed at the start of the beam, with 1 cell in between the attachment

points and later with 2 cells between attachment points. The lattice beam was loaded near the tip with hanging weights in 500mg increments up to 1000mg.

Preparing the robot for measurement consisted of assembling the robot, attaching a cable to transmit serial measurements (due to malfunction of the wireless communications module), allowing the robot to attach itself to the structure and ensuring the robot servos were limp. When attaching the robot to the beam, play in rotation was observed at the robot lattice interface due to the gripper and lattice geometries not matching up. Although for this measurement scenario, the rotation of the grippers are not directly used for the measurement, this issue would need to be fixed to allow accurate measurements in other modes. Additionally, movement of the differential joint caused visible slack on one side of the robot. This slack could cause a delay in servo measurement and an effective loss of sensitivity. The tensioning of the cable presents itself an assembly issue; and the routing, clamping, and tensioning of the cable assembly is a major assembly pain point due to the shape and diameter of the cable channels as well as the limited tensioning capability post-assembly.

The robot pose complied with the beam and the change in servo angles were inspected to observe measurement behaviour. Repeated trials showed consistency and repeatability in each individual servo measurement, though the differential drive servo behaviour were found to differ from each other, causing rotation coupling to be measured and pointing to the aforementioned issue in cable tensioning quality. Instead of a single discrete loading step, a continuous measurement could help gauge the resolution and sensitivity of the measurement system and the robot joints through the course of the experiment in the future. Data collection was also easily handled through the digital twin's pose (end-effector/gripper location). For future experiments, streaming/polling the robot sensory data would allow the assessment of the time resolution of the system.

While the jury-rigged experiments showed the material robot system to be an auspicious platform for testing measurement capabilities. As a proof of concept, the preliminary experiment was a success and going through the procedure of setting the material-robot system and the additional experimental configuration helped give direction to future experimental setups.

The experiment has also highlighted three hardware improvement areas which would benefit both measurement and control characteristics of the robot: the cable tensioner, the gripper geometry, and the wireless module. Work was done in all 3 areas; the completed and tested cable tensioner and gripper designs are provided in section 5.2 and section 5.3 below. The wireless module which was failing due to a power converter design was re-designed but not put into production, the details of the design can be found in Appendix C.

5.2 Cable Tensioner Re-design

The cable tensioner system allows the tension of the cables which drive the differential joints to be adjusted after the robot has been assembled. Having control over the tension of the cables can improve the performance of the joint by removing sag, can improve the reliability of the cable system by making cable unwinding less likely, can improve the long term performance of the robot by providing a means of calibration. Hence, the cable tensioner assembly is a feature which deserves attention if differential joint behaviour wants to be improved.

There were a number of issues encountered with the previous cable tensioning system. The first issue is the flexibility of the 3D printed tensioner part, which caused it to impart less tension on the wires. The second issue was that the 3D printed tensioner part often broke due to the high stress it carried. The third issue was that the range of the tensioning

assembly was too small to allow the cables to be tensioned when the initial tension was not already high.

To remedy these issues, the tensioner system assembly was re-designed with linear screw actuator driven pegs, which increased the range the cables could be tensioned. The new design is however wider than the older one, creating a larger bounding box for the robot and limiting the collision-free movement space. One other issue with the new design is the use of long pins due to limitations in time and inventory. The longer pins cause the tensioner peg to bend out of alignment with increasing tension. An iteration on the design with shorter pins and bearings was made to address and alleviate these issues.

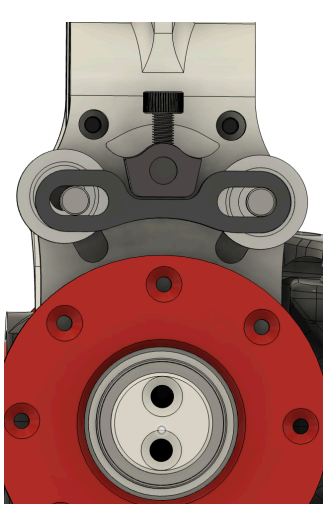

(a) Old tensioner assembly with limited tensioning range

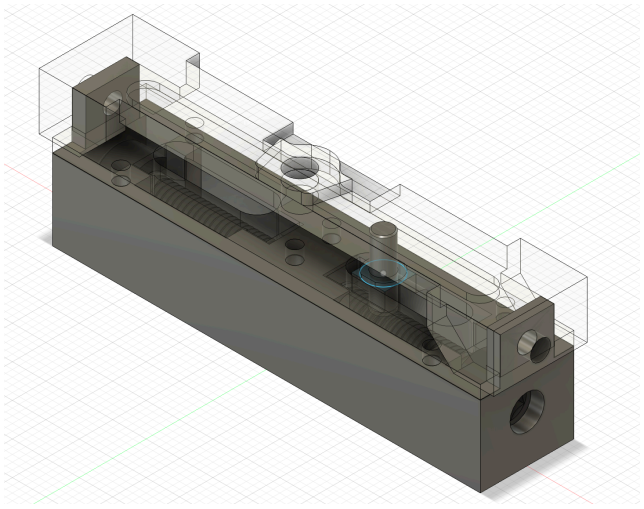

(b) New tensioner assembly featuring screw actuated pegs with larger tensioning range

Figure 5.2: The old and new tensioner designs.

The effect this had on measurement quality can readily be seen by comparing the servo 1 and 2, using the new hardware, to servo 4 and 5 using the old, in Figure 5.3.

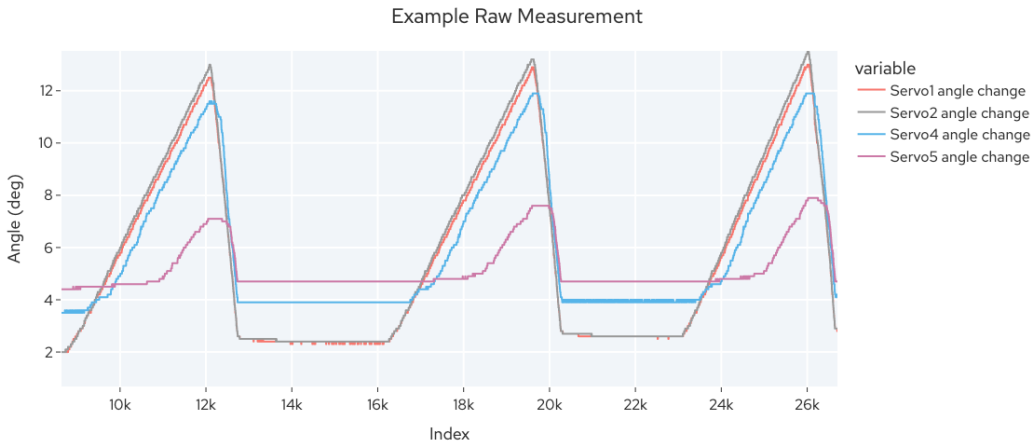

Figure 5.3: Example readings from repeated tests.

Notice on Figure 5.3 how servo 1 and 2 behave much more consistently and suffer much less from backlash compared to servo 4 and 5 thanks to the new tensioner. To quantify, the range of measurements performed with servos equipped with new tensioners are both 11

degrees while the range is only 8 degrees for servo 4 and even worse at 3 degrees for servo 5 for the given measurement with robot on top.

5.3 Gripper Re-design

The gripper is the end effector of the ILLA robot providing alignment to the robot bases. A well designed gripper conforms to the lattice the robot attaches to, providing grip that prevents the robot base from rotating undesirably.

The old gripper had two recurring issues which had to be dealt with.

At one point during the manufacturing of the lattice blocks and ILLAv3 the lattice block geometry was changed to include chamfers on the struts. However, the geometry of the gripper was not adapted. This caused a loose grip which did not align fully and also introduced play once the gripper was docked on the lattice.

The second issue was that the cable assembly was made more difficult due to the narrow channels the cable had to be routed through so they could be fixed with screws.

To fix the first issue, the gripper has been re-designed with the geometry of the lower portion of the gripper changed to match the lattice exactly.

To address the second issue, the cable channels have been made into straight lines and their diameter adjusted so that the cables could be more easily routed while they could still be fixed.

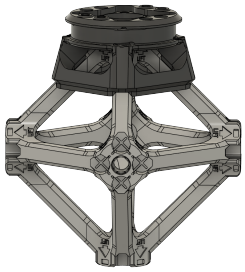

(a) The CAD of the new gripper on top of a lattice.

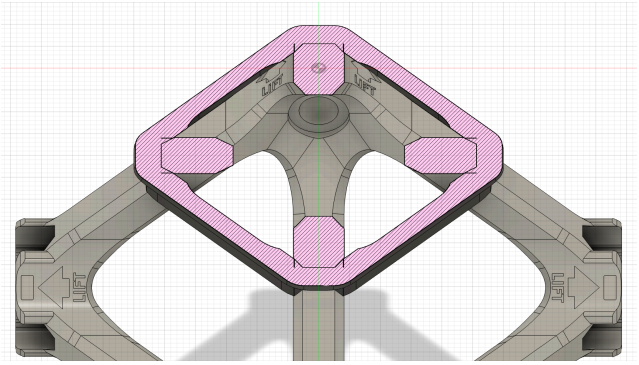

(b) Section view showing new gripper conforming to lattice chamfers.

Figure 5.4: Computer aided design (CAD) models for the new gripper with better fit.

5.4 Assembly and Calibration Plans

The assembly and maintenance of the ILLAv3 was not supported with documentation other than images of the design. To provide consistency and pass on tips and tricks regarding order of (sub)assembly, pre-treatment of parts such as cables, and the software calibration process; a set of articles were written on a lab notebook and handed in along with this thesis.

6

Single Robot Measurement Characteristics

Studying the single robot measurement characteristics is an important step towards assessing the suitability of the robot to be used as a measurement system. The inherent possibilities and limitations of the robot+structure measurement setup form the foundation of inchworm robots as a measurement platform.

Modelling of the measurement signal chain allows for the impact of design parameters such as robot geometry and servo characteristics' impact on measurement performance to be inspected. The theoretical resolution, accuracy, and precision of the robot can be calculated using the measurement chain and the state of the robot+structure. While the system is inherently nonlinear, some factors which cause additional nonlinearities such as loss of sensitivity and saturation also warrant discussion. In some cases, these factors can be curbed with changes to the hardware design as exemplified in chapter 5.

Combined with the knowledge of lattice based cellular structures' properties discussed in chapter 2 and chapter 4, the robot measurement characteristics can be generalized to larger cross-section lattice beams, lattices made out of different materials, or lattices with a different density ratio.

6.1 Degrees of Freedom of the Robot-lattice Structural System

Consider the relative (natural) degrees of freedom of a deforming beam. The tip of the beam can move in 3 axes and rotate in 3 other axes, the corresponding modes are:

- **Stretch/Compression**
- **Vertical Shear**
- **Horizontal Shear**
- **Torsion**
- **Vertical Bending**
- **Horizontal Bending**

The ILLAv3 robot has joints that allow its movements only within the plane spanned by its two main arms. Meaning that the surface normals of the attached lattice blocks must remain within this plane. However, through the rotation of the grippers (attached to the rotation of the differential joint) it can change the orientation of the aforementioned plane, allowing (tracking) movement in 3D space as Figure 6.1 shows.

Figure 6.1: The ILLAv3 movement plane shown in blue and red before and after rotation about the base.

When such a robot is attached to the structure, the joints of the robot allow the tracking of all the singular modes except torsion, since for all cases but the case of torsion the surface normals of the lattice blocks remain in the plane of the robot arms. In case torsion occurs in the structure, the robot mechanisms will not comply with the deformation and will act like a structural member instead. Since the robot is not explicitly designed to take up loads in this manner, torsion poses great risks of failure for the robot and is a significant blind spot of the ILLA robot as a measurement device.

Figure 6.2a, Figure 6.2b, Figure 6.2c illustrate the stretch, horizontal bending, and vertical bending mode behaviour of the robot (at standard position) + beam respectively.

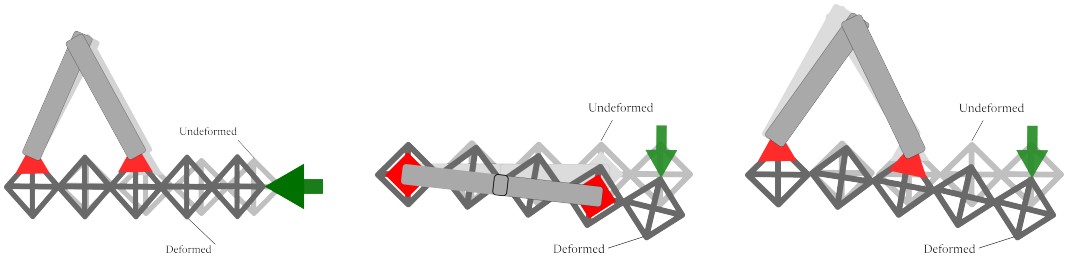

(a) Stretch/compression mode deformation of the beam+ILLA.

(b) Horizontal bending/shear mode deformation of the beam+ILLA.

(c) Vertical bending/shear mode deformation of the beam+ILLA.

Figure 6.2: Illustration of the various modes of behavior for the beam+ILLA system: (a) stretch mode, (b) horizontal bending mode, and (c) vertical bending mode.

6.2 Measurement Chain

Typically, a measurement chain refers to a signal chain of how a sensor signal is treated, processed, and transformed to obtain a measurement signal. We can however expand this idea to illustrate how information gets transformed via mechanical coupling, magnetic sensing, or other means. This gives us an overview of how the information we would like to measure gets transformed and mapped into other information and finally the measurement signal.

The servos which primarily serve to control the robot pose during assembly are each equipped with absolute encoders to track and reference their rotation. When the servos are not in use and ”limp” the encoders continue to provide information about the servo rotation state.

During deformation, the attached robot which complies with the structural geometry experiences a change of pose. This change of pose implies a change in link angles. The link angles are then coupled to the servos with the cable and pulleys in the case of differential joints and screw attachments in the case of the directly driven joint. The encoders in the servos then measure the servo head position and communicate it to an external computer via a serial channel. Figure 6.3 shows the chain of measurement starting with the structural deformation and ending at the computer.

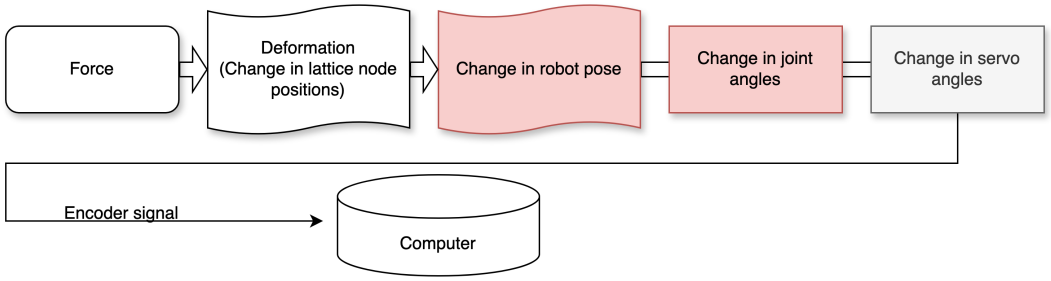

Figure 6.3: The structural deformation measurement chain.

Each step of the measurement chain can be thought of as a transformation of a state with the previous step as an input. The force for example can be transformed to a set of node deformations with the use of the Euler-Bernoulli beam model and knowledge of the undeformed state. The nodes at which the robot is attached can be transformed to a robot pose given the robot geometry and kinematic transformation matrix (inverse kinematics). The robot pose is equivalent to a set of joint angles given the robot link lengths. Finally, the joints are connected to servos via a mechanism which applies a gain and maps the angle to each servo rotation. Finally, these rotations are measured with an absolute magnetic rotary encoder and transferred to a computer to be analysed.

Our goal can then be stated as: given the encoder signal collected by the computer, invert the transformations to obtain the relative deformation of the nodes attached to the robot.

In the case of the servo angles being transformed to joint angles, mechanical leverages (gains) and a reference of what one set of servo angles corresponds to a known set of joint angles (offsets) can be used to obtain the joint angles. The pose (or the location of one gripper relative to the other) can be obtained by performing a forward kinematics transformation as explained in section 4.3. Note that this is inherently a non-linear transformation with trigonometric terms. (It could be linearized about the undeformed pose to provide linear gains for small deformations, however for this thesis project this was not done. The effect of these gains are discussed qualitatively in section 6.3.) The resulting location and orientation

of the two gripper nodes could then be used to define a deformation measure by comparing it to a measured or expected undeformed relative location and orientation. Finally, the problem of estimating external forces and deformations at other points in the structure is not an easy task because the transformations do not map one to one and are not inherently reversible. That is to say that there are many possible combinations of external point forces, distributed forces and moments that could cause the same internal stresses and deformation of the measured nodes, the information of the two nodes does not guarantee information of the other node positions and orientations and much less the force causing the deformation. Therefore, estimating an external force/load requires additional assumptions.

6.3 Single-mode, Statistical Tip Deflection and Load Estimation Model

Consider the problem of estimating the location of the tip of the beam ahead of the robot in a statically loaded deformed structure. In the spirit of data based models, a black-box linear statistical model can be constructed which maps an estimator quantity to accurate tip deflection and load measurements obtained experimentally. The estimator can be constructed from the servo measurement data. There are 5 servo angles being monitored and therefore many estimator candidates. Measurements of any one of the 5 servo angles could be used individually, all the measurements combined, or some combined and others discarded. In this study, we considered the use of two sets of candidates.

The first is the use of a joint angle. For the ILLA robot which features two differential drive joints, two out of 3 movable joints are obtained by combining the differential servo pair measurements, only the mid-joint is directly driven. For the experiments with the robot placed on the side of the beam, the robot differential pair servos moved primarily in differential mode allowing the robot plane to rotate to include the attachment points, while servo 3 recorded a significantly smaller amount of change as expected. For this reason, the joint angle for the first joint which combines the first two servo angle measurements was chosen as the estimator for the case where the robot structural system experiences loads in the horizontal shear and bending mode. The downside of this choice is that only the first two servo measurements are made use of, potentially discarding useful data from the other servos. A second downside is that the chosen servos are all driven with cables which adds another source of uncertainty.

The second candidate is the relative gripper locations or orientations. In this case, all servo measurements are combined within the robot pose calculations to find the coordinates and slope of the connected lattice cell. Within this category, there are many quantities which deserve attention: the most obvious choice would be the use of the vertical displacement of the connected lattice cell. However, for this case, the servos measuring for joints earlier in the kinematic chain would have a far greater effect on the position coordinates than the servos late in the kinematic chain. A second choice would be the slope of the connected lattice. All joints angles contribute to the tip slope equally. Finally, the magnitude of the relative position being measured can also be used. This choice weights the directly connected servo 3 more heavily due to the comparatively long links adjacent to this joint. The magnitude was chosen as the estimator for the vertical bending mode deflection and force estimator because it combines all measurements while weighting the directly connected servo measurement heavier than the elastic joints and is a quantity that can also be used for axial stretch deformations.

6.3.1 Theoretical Characteristics of Estimators

A simplified beam and robot model similar to the one found in section 6.5 can be used to assess the theoretical characteristics of the chosen estimators. A diagram depicts the model in an undeformed state Figure 6.4.

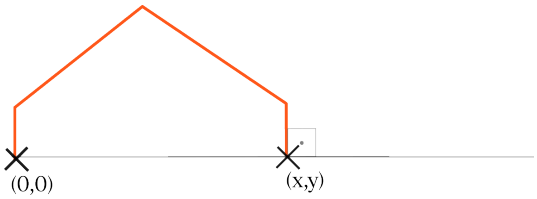

Figure 6.4: An illustration of the simplified beam and robot model.

The model can be used to determine the effect of each servo angle measurement on the estimator when the robot is at its designated pose. Since the individual servo measurement characteristics such as accuracy, resolution, and range are known; these can be translated to the overall measurement system. For example in the case depicted in Figure 6.4 with the robot on top of the beam in standard position, the differential servo pairs' angles can be varied by the resolution amount, then the effect on the estimator (in this case the magnitude of the vector pointing from one robot base to the other) can be calculated. This can be done with the two differential servo pairs as well as the directly driven joint 2 servo to obtain three resolution values. The largest of the three will be considered the resolution of the overall system and the sum of the three resolutions will be defined as the worst case sensitivity of the system.

Table 6.1: Servo measurement characteristics for the HT1 smart servo as provided by the manufacturer LSS.

Characteristic	Reported Value
Accuracy	±0.2 °
Resolution	1/10 °

Table 6.2: Calculated characteristics for the magnitude and tip angle estimators for the vertical and horizontal bending modes, respectively.

	Vertical Bending (Magnitude Estimator)			
Pose	0	1	2	3
Accuracy	0.7879 mm	0.7173 mm	0.5763 mm	0.1924 mm
Resolution	0.3940 mm	0.3586 mm	0.2882 mm	0.0962 mm
Worst Case Sensitivity	0.4578 mm	0.4225 mm	0.3521 mm	0.1601 mm
	Horizontal Bending (Tip Angle Estimator)			
Pose	0	1	2	3
Accuracy	0.1200 deg	0.1200 deg	0.1200 deg	0.1200 deg
Resolution	0.0600 deg	0.0600 deg	0.0600 deg	0.0600 deg
Worst Case Sensitivity	0.0645 deg	0.0645 deg	0.0645 deg	0.0645 deg

Notice how the differential mode joint estimator results are independent of pose, however wider poses would still be beneficial to measurement by increasing the measurement range effectively making accuracy, resolution and worst case sensitivity better.

It must be mentioned that while the 3 apart configuration is theoretically the best performing, it has an upper measurement range limited to 3mm of deflection since the robot reach limit is 403 mm and the robot starting position is 400 mm. Deformations beyond the robot reach limit would saturate the measurement and put strain on the robot.

6.3.2 Measurement Strategy

The beam+robot structural deformations modes were discussed in section 6.1 and can be seen in Figure 6.2. Assuming that deformation occurs only in a single mode at a time allows a measurement strategy to be devised to determine the mode of deflection and then apply a suitable statistical model to obtain estimate deformations.

Looking at the changes in robot pose caused by each deformation, the change in joint angles and servo angles these deformations will cause can be determined. Each deformation mode triggers their own set of joint angle changes, and certain metrics can be used to determine the mode of deformation being observed by the robot.

Figure 6.5 shows a beam deforming in stretch mode with the robot on top. In this case, the base heights will be the same and there will be no slope difference. Servos 1,2 and 4,5 differentially driving joint 1 and 3 will move in tandem mode rotating the joints in opposite directions. Joint 2 will rotate to conform to the changing length.

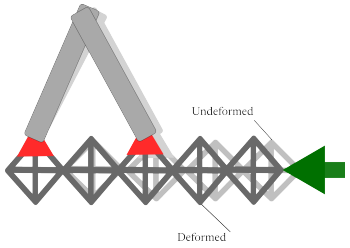

Figure 6.5: Illustration of compression mode deformation.

Figure 6.6 shows a beam deforming in vertical bending/shear mode with the robot on top. In this case, servos 1,2 and 4,5 will move in tandem mode rotating joints 1 and 3 in the same direction. Joint 2 will rotate to open or close the arms depending on whether the robot is on the stretching or compressing side of the bending beam.

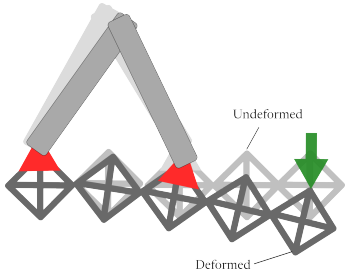

Figure 6.6: Illustration of vertical bending/shear mode deformation.

Figure 6.7 shows a beam deforming in horizontal bending/shear mode with the robot on top. In this case, the robot plane will change. Servos 1,2 will move in differential mode moving joint 1 to rotate the robot plane and servos 4,5 will rotate joint 3 to comply with the difference in slope in the two attached lattices. Joint 2 is expected to not rotate significantly.

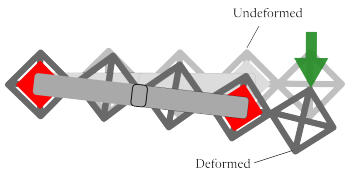

Figure 6.7: Illustration of vertical bending/shear mode deformation.

Since the expected behavior of the joints is known a decision tree can be conducted to determine the mode of deformation as shown in Figure 6.8

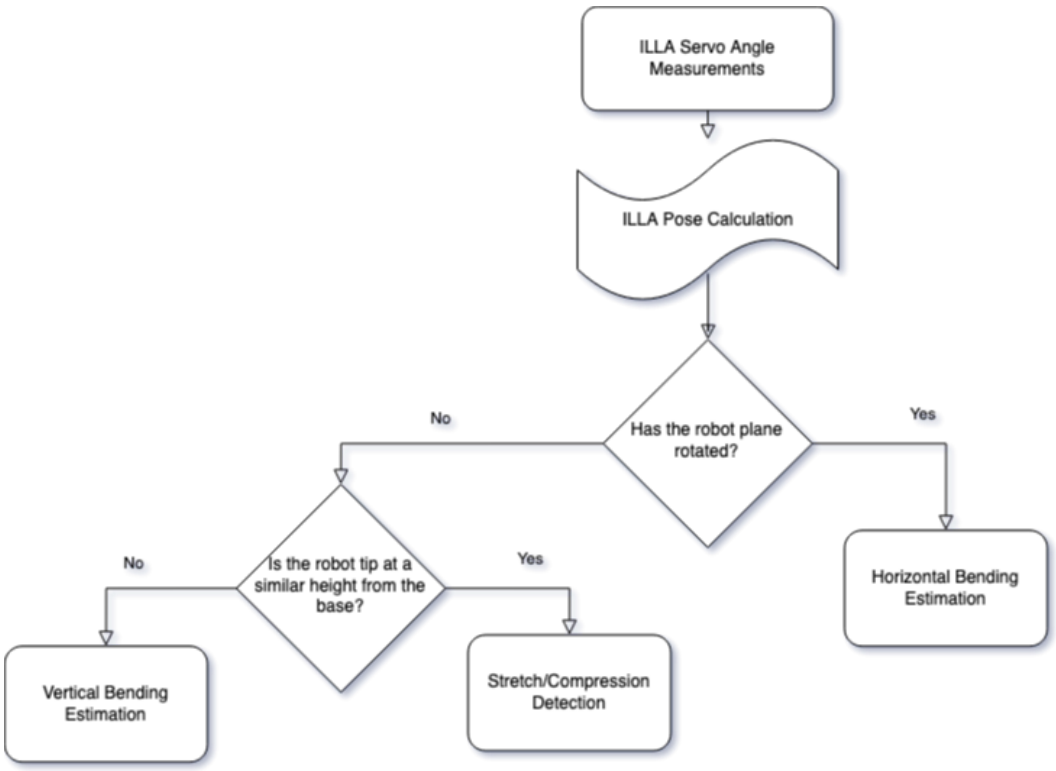

Figure 6.8: Flowchart showing the decision tree to determine the mode of deformation.

Once the deformation mode has been determined the model relevant to the deformation may be chosen and predictions of tip force and deformation made.

6.4 Experimentation Plan

6.4.1 Objectives of the Experiment

The objective of the experiment is to determine the measurement characteristics of an ILLA robot on a digital lattice structure. The set of experiments aims to quantify and validate the following hypothesis:

- The ILLA robot can detect and measure deflections of the structure in the space spanned by the allowable movements in the joint space of the robot.
- The backlash of the ILLA measurement system is significantly below the total range experienced during the experiment.
- The backlash can be mitigated by prepending motion in the direction of the final deflection.
- The beam boundary conditions (BCs) determine the effective length of the beam.

6.4.2 Experiments

Cantilever Bending - 1BC vs 2BCs

In this experiment, the lattice beam undergoes cantilever bending, at 5 lattice length with the root lattice being constrained on the bottom and left node (see Figure 6.9a) and at 4 lattice length with the root lattice constrained only at the left node (see Figure 6.9b). The deflections measured in the tip are then used to compare if the 2 BC case gives an effective beam length reduction.

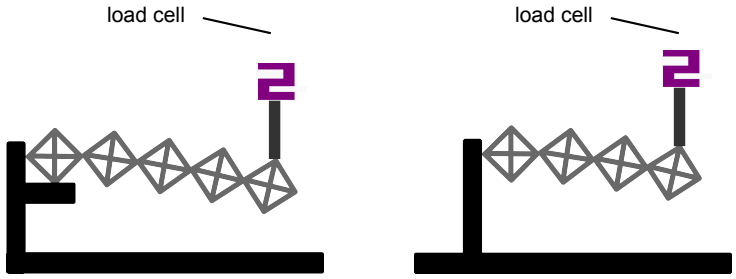

(a) Cantilever beam of 5 lattices with 2 boundary conditions (BCs).

(b) Cantilever beam of 4 lattices with a single boundary condition (BC).

Figure 6.9: Illustration of the test setup with cantilever beams of different lengths and boundary conditions.

Cantilever Bending - Robot on Top

In this case, the structure undergoes deflections and rotations in the robot plane (rotation vector pointing in the plane normal direction). The robot joint 3 rotates the arms to match the relative displacement between the nodes, while the differential joints move in tandem mode to rotate the grippers to match the angles of the lattices.

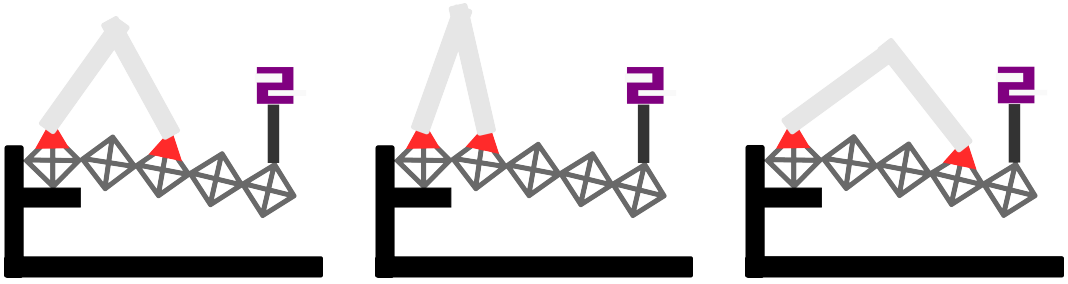

(a) Robot on top in the standard pose.

(b) Robot on top with no lattices in between.

(c) Robot in extended pose (2 lattices apart).

Figure 6.10: Illustration of the test setup with various robot poses with robot on top of the beam.

Cantilever Bending - Robot on Side

In this experiment, the structure undergoes deflections and rotations in the robot ground plane. The robot differential joints move in opposite mode to rotate the grippers to match the lattice rotations.

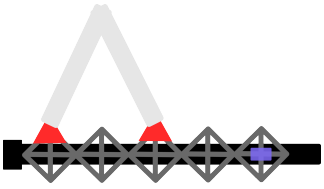

Figure 6.11: Illustration of the top view of the test setup with the robot on the side in its standard pose.

6.4.3 Details of the Experimental Setup

For each experiment, a lattice beam is tested with all lattices oriented with their print direction upwards. The lattice beam is attached to an aluminium frame which is bolted to a 20kN Zwick testing machine with 4 bolts at the baseplate location. The machine applies the displacement/load by moving the base upwards towards the fixed top rod.

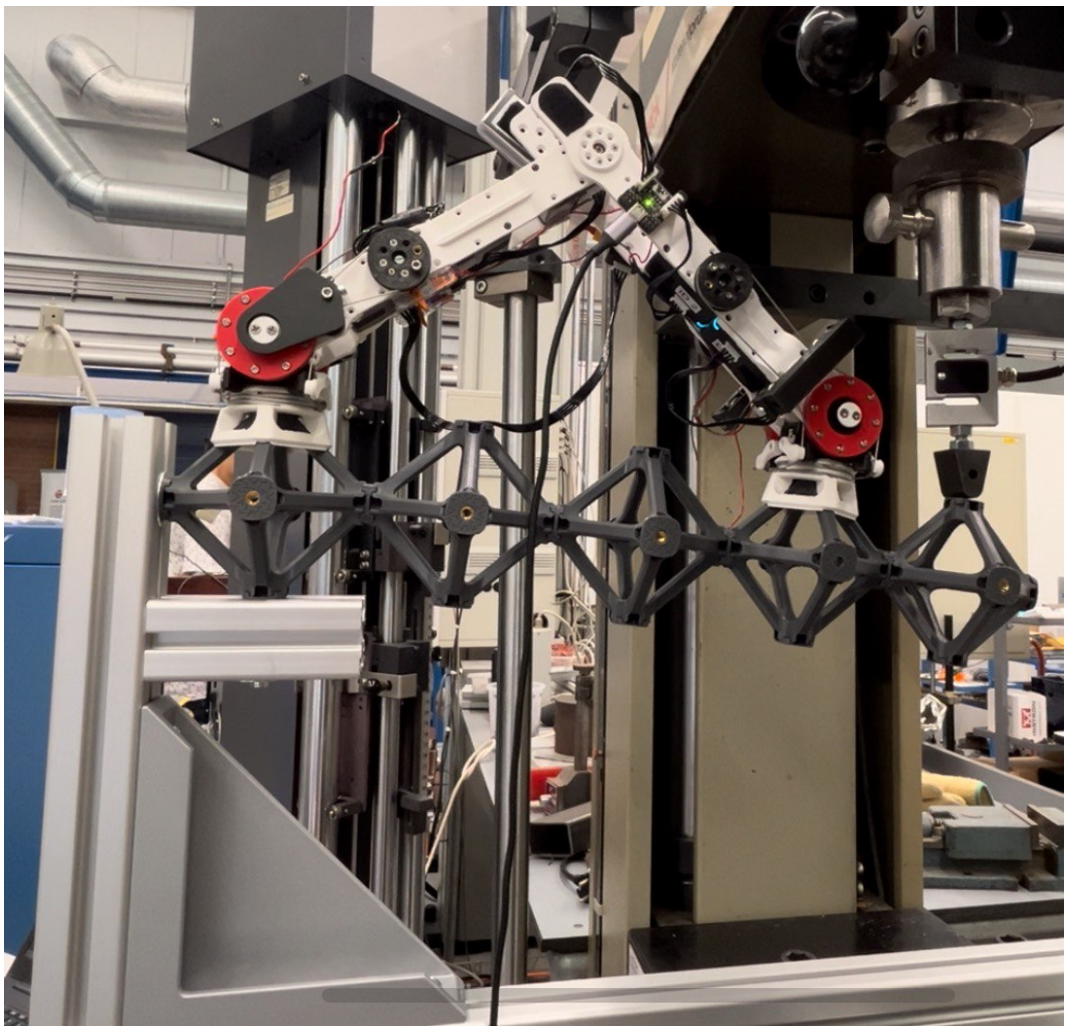

Figure 6.12: A photograph showing the experimental setup with the robot on top.

The top rod consists of a 100 N load cell is used to measure the load at contact point and an attachment with a cylindrical tip (V shaped with a rounded bottom). Due to the bending deformation, the contact point of the tip used to introduce the load shifts a couple of millimetres backwards relative to the beam. The robot is fixed at its location using the built-in gripper screws, the 12 V supply for this operation was provided externally with a laboratory power supply. The servos were powered by battery through the course of the experiments. Data transfer was done through a serial channel via a cable. The Zwick machine was set to measure until 60 mm deformation (measured from the location where the load cell measured a 0.1 N force) or 20 N of force, whichever came first.

6.4.4 Schedule

Experiments take about 3 minutes to run, the resetting of the setup to its starting position takes about 2 minutes, and preloading takes about 1 minute. The list of experiments is presented in Table 6.3 below.

Table 6.3: List of conducted experiments.

Experiment	Variant	Repetitions	BC
1BC vs 2BC	4 lattice	3	1
1BC vs 2BC	4 lattice	2	2
1BC vs 2BC	5 lattice	3	1
1BC vs 2BC	5 lattice	3	2
Robot on Top	STD	5	2
Robot on Top	PM	4	2
Robot on Top	2 apart	4	2
Robot on Top	0 apart	4	2
Robot on Top	0 apart + PM	4	2
Robot on Top	2 apart	2	2
Robot on Top	2 apart + PM	4	2
Robot on Top	2 apart + BS	4	2
Robot on Top	2 apart + BS + PM	4	2
Robot on Top	O(1) 2 apart + PM + BS	4	2
Robot on Side	BS	4	2
Robot on Side	BS + PM	4	2
Robot on Side	STD	4	2
Robot on Side	PM	4	2
Robot on Side	3 apart	1	2
Total		67	

The experiments took place during 8 half days during the first week of September 2024.

Before the first listed experiments, one day was dedicated to a number of trial runs with the aim of calibrating the machine and finding the limit load and deflections at which the beam would fail. The 5 lattice beam failed at 22 N tip force in bending.

6.5 Observations

Backlash & Friction

Some robot measurements and especially the differential joint servos using the old tensioners have shown a lag in measuring deflections. During the pre-moved experiments the effect was more subdued, indicating a dependence of measurement on system history or hysteresis. In an investigation to uncover the cause of this effect the robot joints were studied.

Cable driven robot joints are referred to as elastic joints in robotics. In such as system the cable on one side of the pulley must reach a tension higher than the cable on the other side to create a net moment about the pulley and initiate movement. When and if the pulley movement wants to be reversed, there will be a delay in movement caused by the need to build up enough tension to create the torque to move the joint. The pulley and cables are illustrated in Figure 6.13.

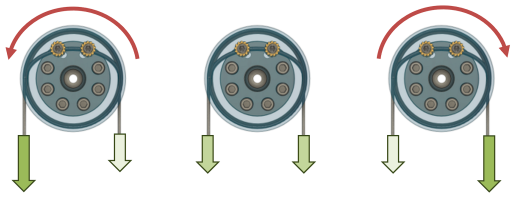

Figure 6.13: Illustration showing reversal of tension on the cable around a pulley mechanism.

During non-pre-moved experiments, the initial conditions of the first trial differ from the second, third, and fourth as seen in Figure 6.14. Furthermore, it was observed that there was a 8-14.5 mm difference in initial tip deflection conditions between the first non-pre-moved trial and the rest. The beam not fully recovering to its initial condition elastically as observed during the beam only experiments shows that the addition of the robot is preventing the recovery of the beam.

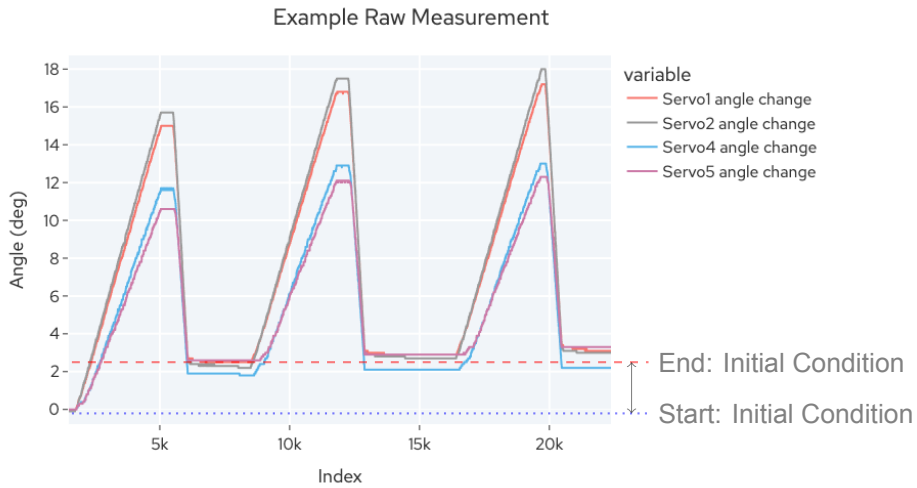

Figure 6.14: Plot showing measurements taken during 4 consecutive runs without pre-movement.

This observation has been attributed to the friction of the servos and robot joints which prevent the recovery of the beam below a tip force corresponding to 4 Newtons (calculated using 12 mm mean tip displacement).

Robot weight

The mass of the robot was measured to be 1075 grams at the last day of experiments. The weight of the robot is therefore $1075 \times 10^{-3} \cdot 9.80665 = 10.54N$. Since the tip force throughout the measurements has remained between 0 and 20N, the robot weight is a significant factor in the behavior of the beam. However, the measurements and predictions are based on relative changes occurring with the introduction of a tip deflection. Therefore, if the robot weight is to be considered a constant factor independent of the tip deflection, the starting point the experiment would be the robot+structure equilibrium position and there would be no effect on predictions. However, while the robot weight is constant, the center of gravity of the robot shifts slightly (magnitude depending on robot pose and location) when the beam bends.

A simplified theoretical model of this problem (with the robot in the 1 apart pose) could be constructed by considering the lattice beam a constant cross section Euler-Bernoulli beam, and the robot as a 4 link mechanism with mass distributed homogeneously along the links. An illustration of the robot pose for the simplified problem is shown in Figure 6.15.

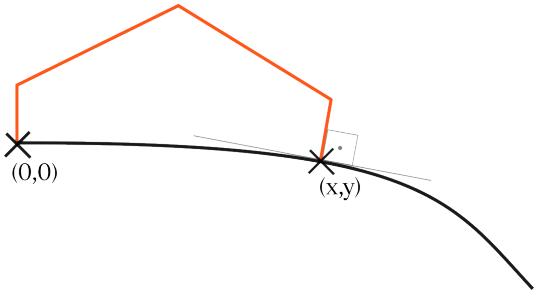

Figure 6.15: Robot pose on the simplified beam problem.

We can then calculate the tip deflection contributions of the robot weight and tip force by substituting the force locations $l/2$ and l:

$$\delta_{\text{tip}} = \frac{5P_{\text{robot}}l^3}{48EI} + \frac{P_{\text{tip}}l^3}{3EI}. \tag{6.1}$$

From this equation it can be seen that if the force due the robot is a constant the tip deflection will a linear function of the tip force with a constant offset. However, if P_{robot} is a function of P_{tip}. The situation is different. The robot force on the beam $P_{\text{robot}}\,(P_{\text{tip}})$ can be calculated by finding the robot pose for a given tip deflection, finding the robot centroid, and calculating the vertical reaction force on the right leg of the robot beam connection.

To calculate the robot pose, the angle (slope) at the robot right leg location and the location coordinates must be found. For the standard robot configuration $x = l/2$. Similar to what was done on Equation 6.1, the equation of the y coordinate at this point on the beam can be found with:

$$y_{l/2} = \frac{P_{\text{robot}}l^3}{24EI} + \frac{5P_{\text{tip}}l^3}{48EI}. \tag{6.2}$$

The slope at the same point is given by:

$$\theta_{l/2} = \frac{P_{\text{robot}}l^2}{8EI} + \frac{3P_{\text{tip}}l^2}{8EI}. \tag{6.3}$$

The robot link dimensions are 30.5 mm, 201.5 mm, 201.5 mm, 30.5 mm. With these all but joint 2 locations are known. The joint 2 coordinates can be found trigonometrically using the link dimensions and the joint 1 and 3 locations. The expressions for the resulting joint locations are shown in Table 6.4.

Table 6.4: Solutions for the joint coordinates for the robot pose for the simplified beam problem.

Joint	Position
0	(0, 0)
1	(0, 30.5)
2	$(J2_x, J2_y)$
3	$\left(\frac{l}{2} + 30.5\cos(\theta_{l/2}), y + 30.5\sin(\theta_{l/2})\right)$
4	(x, y)

The centroid of the robot can then be calculated using the robot pose and the x coordinate of the centroid used in determining the reactions.

$$R_2 = P_{\text{robot}} = \frac{x_{\text{centroid}}}{l/2} \cdot g \cdot m, \tag{6.4}$$

where g is the gravitational acceleration and m is the mass of the robot.

Solving for the tip deflection assuming an elastic modulus of 3019 MPa (3D printed PLA) and a second moment of area of 5300 mm^4 (examples), we obtain the robot force contribution in Figure 6.16.

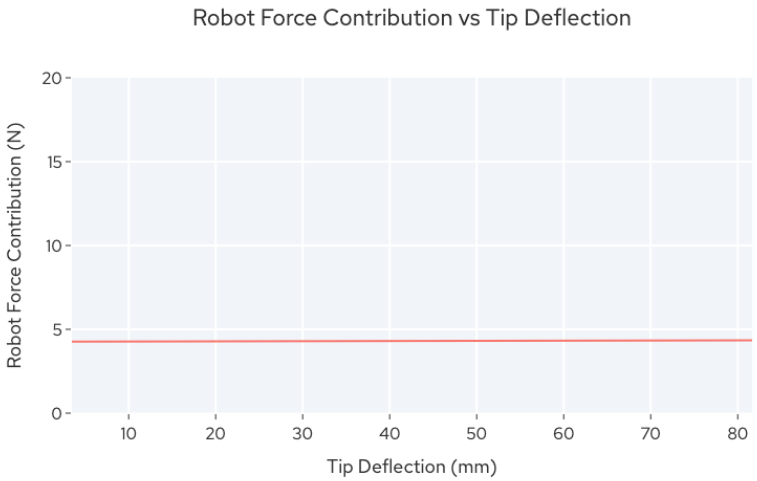

Figure 6.16: Simulated robot force contribution.

The robot force contribution does increase with increasing tip deflection but the increase is only 0.08 N over the measurement range, justifying the assumption that it can safely be considered a constant during the model construction stage.

Relaxation of the beam after trials

The load cell measuring the tip force has shown to measure a steep decrease in load with time after each trial when the trial was over and the tip was kept at the maximum deflection point. The rate of decrease decayed with time. Since the machine was not set to do cyclic testing the setup did not record this relaxation of the robot beam system. Due to time constraints, the research into the cause of this behaviour has been left for future work.

6.6 Results

6.6.1 Beam only measurements

The measurements on the beam alone allows us to determine the bending stiffness of the single lattice beam and compare the effective stiffness of the beams with different lengths and boundary conditions.

Figure 6.17, Figure 6.19 and Figure 6.18 show plots of tip deflection vs tip force for lattice beams.The slopes of the curves were calculated using the strains closest to 5% and 20% of the measurement range.

$$\frac{F}{\delta_{\text{tip}}} = \frac{F_{20\%} - F_{5\%}}{\delta_{\text{tip}_{20\%}} - \delta_{\text{tip}_{5\%}}}. \tag{6.5}$$

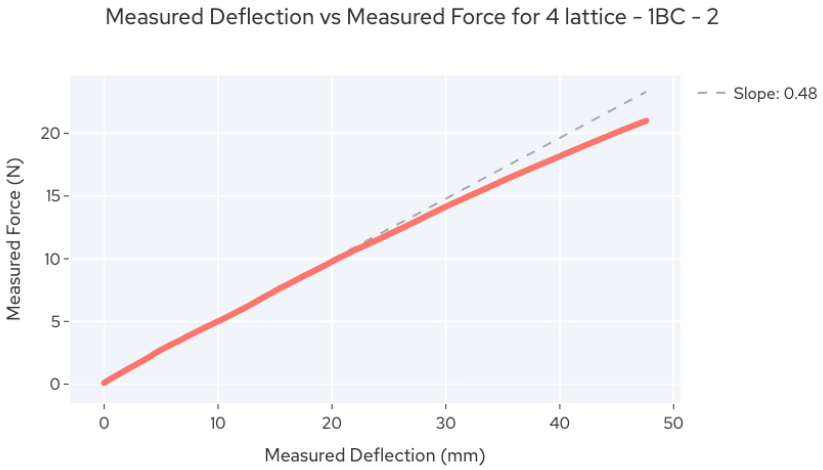

Figure 6.17: Tip force vs deflection for 4 lattice beam with a single BC

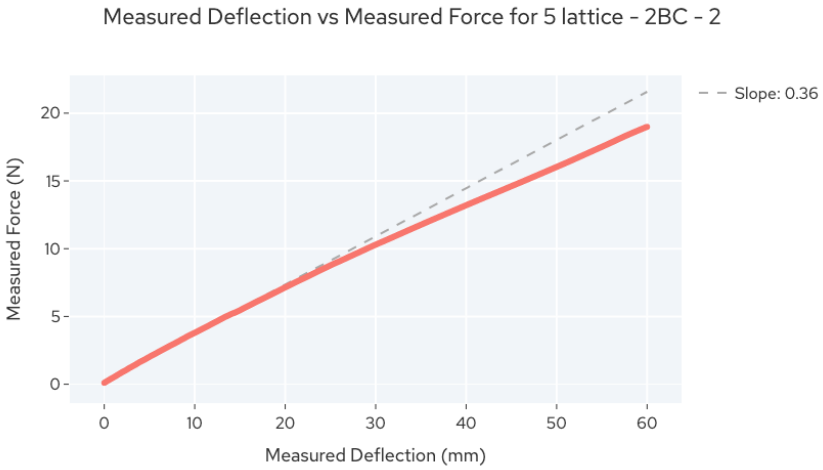

Figure 6.18: Tip force vs deflection for 5 lattice beam with 2 BCs

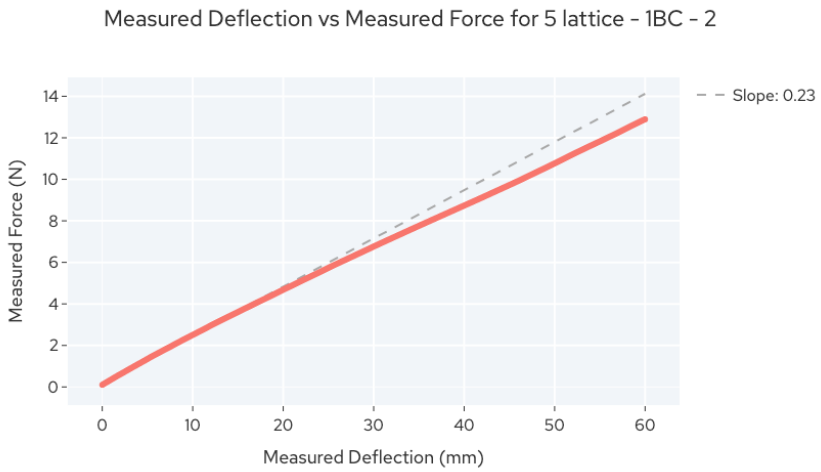

Figure 6.19: Tip force vs deflection for 5 lattice beam with 1 BC

As expected the introduction of an additional boundary condition causes the beam to be stiffer. However, the stark difference in slope between the 5 lattice 2 boundary condition (BC) result and the 4 lattice single BC result shows that adding a second BC can not be considered equivalent to reducing the beam length by a single lattice. The additional BC constrains one out of 12 beams that make up the octahedron completely (from both sides) and adds a single side constraint to three more beams. The remaining unconstrained beams and the single side constrained lower beams still deform and therefore contribute to reducing the stiffness beam stiffness.

Furthermore, a noticeable decrease in stiffness (softening) is measured between the 20 mm and 30 mm tip deflection points. Beyond 30 mm the beam stiffness settles at a lower value until beam failure.

Equivalent elastic modulus calculation

The single boundary condition deflection results can be used to calculate an equivalent elastic modulus by using the Euler-Bernoulli beam model given by the following equation:

$$\delta_{\text{tip}} = \frac{FL^3}{3EI}. \tag{6.6}$$

Rearranging the terms yields:

$$EI = \frac{F}{\delta_{\text{tip}}}\frac{L^3}{3}. \tag{6.7}$$

Table 6.5: Experimental stiffness results.

	L	$\frac{L^3}{3}$	$\frac{F}{\delta_{\text{tip}}}$	EI	E
4 lattice beam (1 BC)	350	1.43×10^7	0.48	6.86×10^6	823 kPa
5 lattice beam (1 BC)	450	3.03×10^7	0.23	6.92×10^6	838 kPa

The beams are considered of length 350 mm and 450 mm respectively since the tip force is applied at the centre of the lattice at the tip reducing the length by 50 mm. The average equivalent elastic modulus results in 830 kPa.

Equivalent length for the 2 BC case
Using the calculated equivalent elastic modulus $E = 830$ kPa, the chosen second moment of area $I = 100^4/12$ mm^4, and the two boundary condition results for the 5 lattice beam, we can construct a similar relationship with an effective length L_{eff}:

$$\delta_{\text{tip}} = \frac{FL_{\text{eff}}^3}{3EI}. \tag{6.8}$$

The effective length can be calculated with

$$L_{\text{eff}} = \left(\left(\frac{F}{\delta_{\text{tip}}} \right)^{-1} \cdot 3EI \right)^{\frac{1}{3}}. \tag{6.9}$$

The resulting effective length is 386 mm. The starting point of the beam would then approximately correspond to the robot attachment location validating the simplified model used in section 6.5 during the estimation of the robot weight effect. (14mm ahead of the gripper attachment (3.6% difference)).

6.6.2 Linear statistical models

As an example of a purely data based model, a statistical estimator is constructed. Given an observed or derived estimator and the measured quantity that wants to be estimated, a linear relationship can be set up of the following form:

$$E(f) = B * (f + A), \tag{6.10}$$

where f is the estimator, $E(f)$ is the estimate, B and A are constants that minimize the error between the estimate and measured values using the least squares method.

Two examples of the model construction steps, chosen at random for a magnitude based estimation model with the robot on top and a tip angle based estimation model with the robot on side are provided in Figure 6.20, Figure 6.21 respectively.

Each figure consists of six plots divided into 3 rows. The first row consists of the preprocessing of collected data. The first plot shows the raw angle data collected from the ILLA robot servo encoders. The second plot shows the calculated estimator. In the case of Figure 6.20 the estimator chosen is the magnitude of the distance between the two grippers, obtained by processing the servo angles into a robot pose geometry. From this estimator two statistical models are constructed: one for the estimation of tip deflection and another for the estimation of tip force.

The second row plots correspond to the tip deflection estimation. The third plot shows the tip deflection estimate and the deflection measurement, the outcome of the estimation. The fourth plot shows the error of the deflection estimate vs the measurement progress, the error behaviour of our estimation.

The last row corresponds to the tip force estimate. The fifth plot shows the tip force estimate and the force measurement, the outcome of the tip force estimation. Finally, the sixth plot shows the error of the force estimate vs the measurement progress. The measurements compared are obtained from the Zwick 20 kN testing machine.

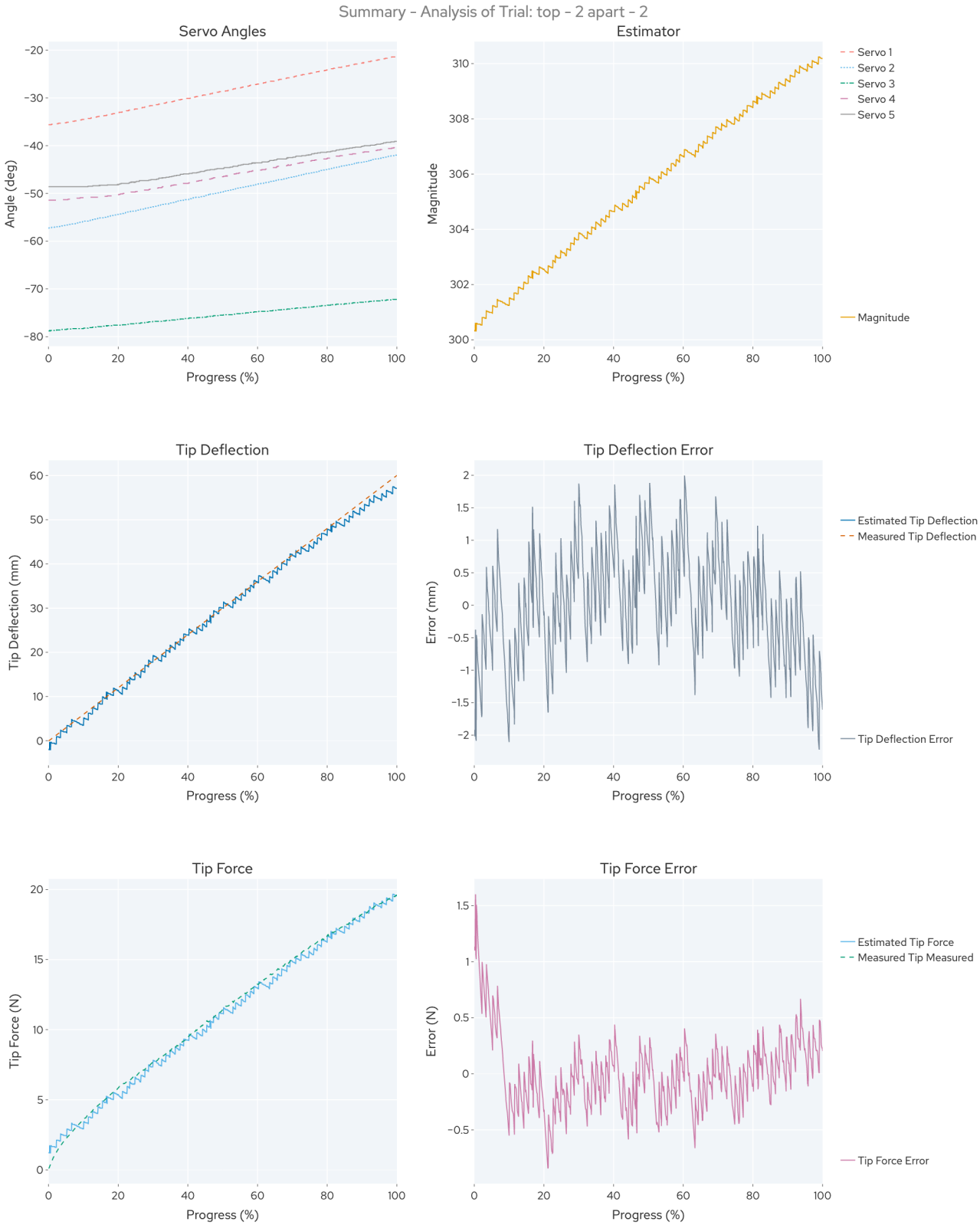

Figure 6.20: Model construction process, robot on top.

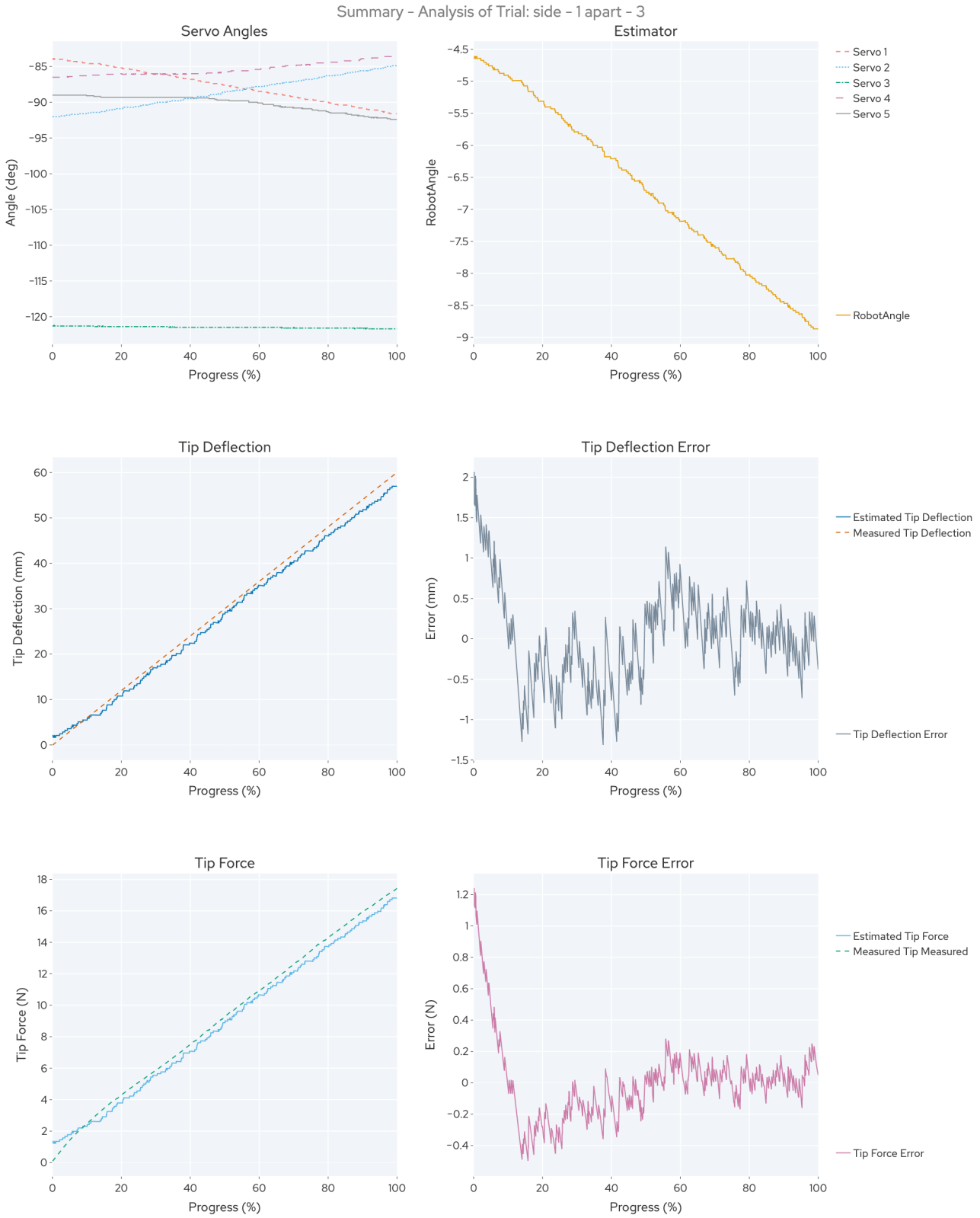

Figure 6.21: Model construction process, robot on side.

Notice how the error for measurements (shown in Figure 6.21 & Figure 6.20) are higher initially and over the course of the experiment trail down. This is due to the elasticity of the joint causing a loss of sensitivity at the start of experiments similar to backlash found in geared mechanical systems. Also notice that the force estimate is also inaccurate at the start due to a non-linear softening over the course of the experiments.

To summarize all the statistical models generated from experimental results, Figure 6.22 includes box and whiskers plots showing the error mean and standard deviations for the models constructed to estimate the tip deflection while Figure 6.23 shows the box and whiskers plots for models constructed to estimate tip force. Note how most errors have a mean smaller than ± 1 mm. The standard deviation of the errors are also typically below 1 mm. A clear trend is observed where the choice of wider pose decreases both the error in measurement and standard deviation. Also observe how the side measurements show the choice of estimator and measurement mode impact the measurement quality.

(a) Error means

(b) Error standard deviations

Figure 6.22: Error mean and standard deviations for the tip deflection estimates.

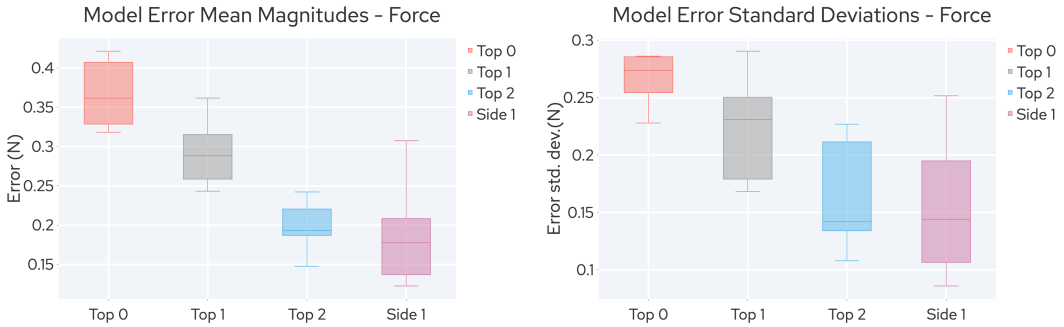

(a) Error means

(b) Error standard deviations

Figure 6.23: Error mean and standard deviations for the tip force estimates.

The estimator, like the servo angle measurements it is derived from, exhibited discrete measurement behaviour. This in turn caused the error to oscillate. Figure 6.24 shows examples of errors for estimates in three different robot poses.

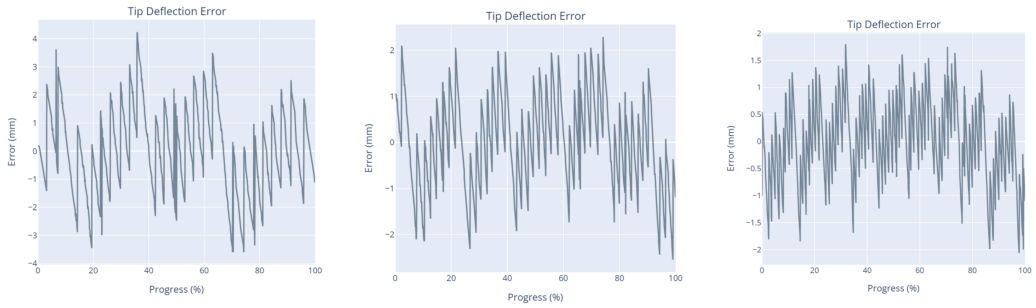

(a) Error for 0 apart pose **(b)** Error for standard pose **(c)** Error for 2 apart pose

Figure 6.24: Plots of error behaviours for different poses for the vertical bending deformations.

The error shows two distinct oscillations, one high frequency and one low frequency. Furthermore it appears that changing the pose has a direct effect on both frequencies yet relative to each other they retain an approximate 1:7.5 ratio. Further investigation shows that the high frequency mode is correlated to the resolution of servos while the lower frequency is caused by cables of differentially driven joints wrapping over itself and falling into the bed of the pulley groove periodically at the pulley edge.

6.6.3 Generalizing the Theoretical Results

Let us define a detectable deformation mode as a mode for which the measurement system provides estimates with a resolution of at most half that of the measurement range; i.e., the system measures at least two data points before the beam yields. Similarly, let us define a measurable deformation mode as a mode for which the measurement system provides estimates with resolution at least one tenth of the measurement range; i.e., the system measures at least 10 data points before the beam yields. This allows us to create the following detectability and measurability thresholds:

- Detectable Deformation:

$$2 \times \text{Resolution} \leq \text{Estimator change at yield } (D_d) \tag{6.11}$$

- Measurable Deformation:

$$10 \times \text{Resolution} \leq \text{Estimator change at yield } (D_m) \tag{6.12}$$

The maximum stress of a Euler-Bernoulli beam subjected to a vertical tip force occurs at the root of the beam and is calculated with:

$$\sigma_{\text{max}} = \frac{M_{\text{root}} \cdot h/2}{I} = \frac{P_{\text{tip}} L \cdot h/2}{I}. \tag{6.13}$$

For a given yield stress for the beam, the tip force equivalent will be different for larger cross-section beams due to higher second moment of area I and higher beam cross-section height h. For a 2x2 lattice beam the height will be two times greater and the second moment of area I will be 16 times greater, meaning a tip force P_{tip} 8 times higher will be required to yield a 2x2 lattice cross-section beam compared to a single lattice cross-section beam. For 3x3 lattice cross-section beams, the tip force P_{tip} will be 27 times higher.

The magnitude of deflections at yield will be counter-balanced by the increase in effective elastic modulus due to more connectivity between cell nodes and higher second moment of area as Table 4.1 and Table 4.2 display. The deflection at point x along the beam is given by the equation:

$$\delta_x = \frac{P_{\text{tip}} x^2}{6EI} (3L - x). \tag{6.14}$$

For a 2x2 beam the elastic modulus E is 3.2 times that of a 1x1 beam and the second moment of area I is again 16 times greater. For 3x3 beams, the elastic modulus is 5 times greater and the second moment of area I, 81 times greater. Given that P_{tip} is now larger, the deformation at yield can be shown to be a factor 6.4 lower for a 2x2 beam and a factor 15 lower for a 3x3 beam.

For stretch mode deformations of constant cross-section beams, the stress along the beam length will be constant. Assuming a bulk material with the same yield strength, the deformation caused by the yield stress is given by Hooke's law:

$$\epsilon = \frac{\delta_x}{x} = \frac{\sigma_{\text{yield}}}{E}, \tag{6.15}$$

$$\delta_x = \frac{\sigma_{\text{yield}}}{E} \cdot x. \tag{6.16}$$

The deformation will be 3.2 times lower for a 2x2 beam, and 5 times lower for a 3x3 beam.

While for the stretch mode, the deformation at the robot gripper location δ_{gripper} maps one to one to the magnitude estimator change; for the bending modes this is different.

Downward deflection of a beam at the robot gripper location is linked to the magnitude change of the gripper separation by the Pythagorean relationship:

$$(L_{\text{gripper}} + D)^2 = (L_{\text{gripper}} + \frac{h}{2}\sin(\theta_{\text{gripper}}))^2 + (\delta_{\text{gripper}} - \frac{h}{2}\cos(\theta_{\text{gripper}}) + \frac{h}{2})^2, \tag{6.17}$$

with a small angle approximation,

$$(L_{\text{gripper}} + D)^2 = (L_{\text{gripper}} + \frac{h}{2} \cdot \theta_{\text{gripper}})^2 + (\delta_{\text{gripper}} - \frac{h}{2} \cdot (1 - \frac{1}{2}\theta_{\text{gripper}}^2) + \frac{h}{2})^2, \tag{6.18}$$

where,

$$\theta_{\text{x}} = \frac{Px}{2EI}(2L - x). \tag{6.19}$$

D denotes change in magnitude, L_{gripper} is the initial magnitude of the gripper to gripper separation (how far apart the grippers are on an undeformed beam), h is the height of the beam cross-section. The height of the beam h and θ come into play due to the robot placement on the surface which is offset from the neutral axis.

For the horizontal bending case, the downwards deflection at the gripper location δ_{gripper} is linked to the gripper separation angle θ_{gripper} estimator with a trigonometric relationship:

$$\tan(\theta_{\text{gripper}}) = \frac{\delta_{\text{x-gripper}}}{L_{\text{gripper}}} \simeq \theta_{\text{gripper}}. \tag{6.20}$$

The second part of Equation 6.20 comes from a small angle approximation.

At this point, the estimator changes are calculated using the theoretical estimator resolution found in Table 6.2, Equation 6.11, and Equation 6.12. Given a estimator change thresholds and trigonometric relationships, the corresponding beam deflections which would cause the estimator change are calculated. Using the Euler-Bernoulli beam model, the critical elastic modulus which would exhibit the minimum deformation behaviour required is found assuming a force applied at the beam tip causing a deformation of the beam in a single mode (vertical bending, horizontal bending, stretch/compression (assuming magnitude estimator)). This modulus value is the highest equivalent elastic modulus the material can have which would result in detectable or measurable deformations.

Table 6.6 shows the results of these calculations for the robot on top in a 2 lattice apart pose.

Table 6.6: Summary of measurable and detectable deformations in terms of maximum equivalent modulus (all values in kPa).

	Vertical Bending		Horizontal Bending		Stretch	
	Detectable	Measurable	Detectable	Measurable	Detectable	Measurable
1x1	14950	3140	54076	10815	26519	5304
2x2	14800	3000	8449	1690	8287	1657
3x3	14770	2980	3605	721	5304	1061

This table now serves as a guide to assess how well the robot can measure deformations for a given lattice beam and deformation mode. The previously reported elastic modulus of 830 kPa can be compared directly with the vertical and horizontal bending values in the table. This shows that the measurement system can detect bending deformations for up to 3x3 beams and is able to measure in vertical bending for up to 3x3 beams while it can only measure horizontally up to 2x2 beams.

For the stretch mode, the elastic modulus of beams of 1x1, 2x2, and 3x3 cross section can be calculated by using Gibson-Ashby theory of cellular materials (50.3 MPa) and applying a correction factor for sparse beams (1/18 for 1x1/∞x∞) as documented earlier in chapter 4, resulting in the following theoretical elastic moduli:

Table 6.7: Elastic moduli of sparse beams in the stretch direction in kPa.

Cross-section	E-modulus
1x1	2790
2x2	8942
3x3	13972

Note how the experimentally determined flexural modulus (830 kPa) differs by a factor 3 from the theoretically determined stretch mode elastic modulus (2790 kPa).

Comparing to the maximum moduli reported in Table 6.6 shows that only the detection and measurement of 1x1 beams in the stretch deformation mode are supported.

To conclude, the results show that the robot can detect and measure bending deformations also with larger beam cross-sections. However, it can not measure and detect stretch mode deformations beyond the single lattice beam. Measuring a single deformation point for stretch mode deformations for larger beam sections is rendered outside the robot capabilities also due to the loss of sensitivity at the start of the measurement range, in the same order of magnitude as the resolution.

6.7 Discussion

The results and especially the generalizations made rest on numerous assumptions made throughout this project. The implications of these assumptions and recommendations for future refinements are provided below.

6.7.1 Model choice

There are several models which can be used to estimate relative deflection of the tip given the robot measurements. These include but are not limited to analytical models such as the analytical Euler-Bernoulli beam model in subsection 6.3.1, simulation based models such as finite element analyses, or data based models such as trained neural networks. The statistical data based model chosen in this study provides a simple and accurate model for the estimation of the tip deflection and force, with the limitation of estimating only for the bending deflection mode with the robot locations which were tested for. The research and implementation of different models would be beneficial to solving more general load case and robot pose combinations. For the statistical model used, more elaborate estimators could be constructed and studied. However, for the scope of this exploratory study into the characteristics of contact based robot measurements, the constructed model is instrumental and satisfactory in revealing the possibilities and limitations of data based measurement systems using the ILLA robot. A next step could also be relaxing the constraints based on the scope of this study by for example allowing for more than a single mode of deformation at a time or exploring tensor estimator quantities rather than individual scalars.

When deriving properties such as an effective flexural modulus for the beam, assessing the importance of factors such as the robot weight, or extending the results an analytical Euler-Bernoulli beam model is referred to. Analytical models are useful owing to their simplicity which makes them often times applicable to a broader set of examples. Though the results are likely less accurate than simulations or data based heuristic models, they are more suitable for illustrating ideas.

Fundamentally, all of the materials studied in this report have been assumed to be bulk cellular materials. While the case of completely assembled lattice based structures exhibit cellular properties, it is valid to criticize the applicability of the same model to the sparse 1x1 cell beams studied in this work. While it is evident that these sparse materials behave in a different regime as studied by Jenett for stretch mode deformations of sparse cuboctahedral systems, this work has similarly chosen to analyse the beams in context of the cellular materials they are designed to assemble into [10]. For engineers aiming to implement a contact based robotic measurement system in discretely assembled material-robot systems having the same context could prove valuable. In the future, conducting experimental or simulation studies about the bending/shear behaviour of sparse octahedral lattice cell structures would greatly benefit this work by removing the assumption that sparse octahedral cell structures scale and relate to the cellular bulk material in the same way cuboctahedral cell structures do.

6.7.2 Experiment results

Observations made regarding the ILLA robot and testing machine through the course of experiments have been discussed in section 6.5. The nonlinearities of the system such as dependence on previous state (a form of hysteresis), a loss of sensitivity at the start of movement, and the effect of robot weight are explored in that section. The following paragraph aims to deliberate on the observations of the processed data and results.

The beam only measurements show that the beam stiffness changes after 20 mm of deflection. This could be due to the beam approaching yield in which case the 20 mm deformation point would correspond to the proportionality limit with the beam remaining

elastic until inter layer failure. Another explanation is the presence of pretension in the joint fasteners or the complex anisotropic properties fused filament fabrication imparts on the lattice cells such as internal stresses due to temperature change. This effect warrants being studied further if larger deformations are expected during manufacturing. Similarly the force needed to cause these deformations have also shown nonlinear behaviour which caused the linear statistical estimator to exhibit higher discrepancies in the beginning and end of the measurement ranges.

The measurement data collected for different poses as well as the theoretical calculations in subsection 6.3.1 show that the robot pose is a significant choice which plays a role in determining the resolution, accuracy, and range of measurements. The 2-lattice-apart pose performs the best among the tested poses due to both finer resolution thanks to the effect of robot pose geometry and an increase in node relative deflection thanks to the attached nodes being further apart. The theoretically observed 3-lattice-apart pose is also noteworthy, boasting a resolution 3 times finer than the next best pose; this pose in particular should be studied in case stretch mode deformations of small magnitude are to be more reliably detected and measured. The recommended pose for all bending/shear mode measurements for slender beams is the 2 apart pose.

The location of the robot is also worth discussing. Due to space constraints between the beam and the testing machine, only one pose where the robot is not at the beam root is tested. Due to the highest moments being at the root, the robot also best performs when placed at the root where the relative deformations between the nodes the grippers are attached to are largest. When moved further along the beam, the relative deformation for the cantilever bending case rapidly drops decreasing resolution for the estimate. However this is not considered a major issue since the robot is not confined to one location, it can be made to navigate to favourable locations.

6.7.3 Error Behaviour

The errors in magnitude estimators present themselves in two distinct frequencies as shown in Figure 6.22. The cause of both modes have been identified through calculations and inspection to be due to the measurement resolution and a flaw in the cable system. The resolution of the measurement can be improved by selecting a different estimator as exemplified by the horizontal bending (or robot-on-side) models constructed, by improving the encoder resolution, or by changing the robot pose or design geometry. To remedy the cables wrapping over each other and causing a periodic disturbance by designing an elastic joint system with grooved pulleys to guide the cable and maintain consistent cable lengths between pulleys, similar to the approach of Hwangbo et al. [42]. The design remains a challenge due to the small size and space constraints of the robot.

6.8 Single Robot Measurement Characteristics - Conclusion

The results show that although there is plenty of room for improvement, lattice locomoting assembly robots are good candidates for introducing measurement capabilities and self awareness to the manufacturing process. The collection of robot pose data and by extension structural node location data is a latent resource which comes at no additional cost and can be readily made use of for measuring and detecting deformations of sparse beam sections naturally occurring early in the manufacturing. The extent of the robot measurement capabilities and various phenomena affecting measurement have been explained.

Part III

Discussion


TU Delft
Delft
University of
Technology

7

Conclusion

This thesis project set out to answer the following research questions:

- How can the meso-scale digital structures be made self-aware, completing the structure – digital-twin loop?
    1. What magnitude of deformation can be expected of such a two-scale structure, how does it behave?
    2. Do the ILLA robots have sufficient capability to reliably measure these deformations?
    3. How can the deformation of the overall structure be estimated using a set of local, surface level measurements?

The answer to subquestion 1 has been answered partly in literature by Gibson and Ashby theoretically, and by Jenett and Cheung experimentally for octahedral lattice structures. Their work show how the effective elastic modulus of the structure depends on the base material chosen, the relative density of the lattice cells, and the boundary conditions of the lattice cells (single lattice cell cross-section vs larger cross-sections). Answering this question has allowed the generalization of the measurement assessment of the robot by calculating an expected deformation range for each mode with the effective modulus of the structure and yield strength of the base material.

The answer to subquestion 2 has been answered by assessing the measurement characteristics of the ILLAv3 robot both theoretically and experimentally. The ILLAv3 has been shown to be capable of measuring bending deformations up to beam cross-sections of 3x3 lattices. Axial deformations have also been shown to be possible to measure for single lattice cross-section beams. The nonlinear measurement phenomena observed in experimental measurements have also been discussed, providing improvements and recommendations which can be applied in the future.

The third research question has only been partly answered by constructing statistical tip deflection and tip force estimation models for the given setup. The estimates have been shown to reliably predict the tip deflection within 2 mm accuracy. The tip force showed less linear behaviour and therefore could only be estimated within 2 N accuracy.

Finally, in answering how the meso-scale digital structural systems can be made self-aware, this project can be considered a first step in collecting structural data in these type of digital robot-material systems. Additionally, this project is the first introduction of material mechanics into the current manufacturing system model which assumes rigid bodies. More work undoubtedly needs to be done to provide better and more general self-awareness to the structural system.

8

Future Work

8.1 Significance of integrated measurements

The integration of measurement capabilities to the structural system brings about many possibilities. To start with, it improves the digital twin model by contributing information on lattice positions during traversal, making the digital representation closer to the true structure.

As an extension to this and secondly, it is clear that the self alignment capabilities of the robot don't provide it enough robustness to deal with highly strained slender structures it is likely to encounter during early steps of the construction. The model built here could form the basis of adjustments made to pose manipulation commands during robot traversal to ensure the robot attempts to dock with a lattice at a location estimate closer to the true position.

Thirdly, this study can be considered the first attempt at introducing physics driven system information (elasticity, gravitational forces) for the localization of lattice blocks. Although more work is needed to generalize and implement a physics based system, this information can eventually be used during manufacturing to formulate new physics informed strategies for construction of the structure such as the bending of lattice beams to reach certain positions as seen on the machine learning driven structural manipulation strategy implemented by Kalousdian et al. [30].

Finally, through repeated measurements over time, the lattice block material characteristics can also be determined and the change in their mechanical response monitored. The information obtained from integrated measurements could then contribute to controlling the two-hierarchy optimization process at the material and at the structural level. One way robots can contribute is by continuously monitoring the structure during and after manufacturing; the deformation data can then be used to determine which parts of the structure are more highly stressed. These areas can then be reinforced with additional lattice blocks.

8.2 Robotic measurement systems of the future

It is expected that the assembly robots will be improved in terms of capabilities. It is also expected that the monomorphic robotic system in the future could be expanded to include various different types of robots. More work will be necessary to fuse different modes of measurement information and to plan the positioning and inspection tasks of different robots.

One possible extension to both the current assembly and measurement system is the inclusion of quadcopter agents which are much faster than inchworm robots in traversing the structure. During assembly, quadcopters robots could transport lattice blocks to the

assembly front, saving the ILLA robots time-consuming back and forth trips carrying lattice blocks in large structures. For measurement, quadcopters equipped with cameras can use images to localize themselves as well as coarsely monitor the structure from different angles, identifying locations of interest for more detailed contact based measurements, in a way dictating the coverage path planning for ILLA robots.

While this study is based on the ILLAv3 robot, the aim of this work is to explore and facilitate the re-use of methods and models to characterize and process robotic contact based measurements and should remain applicable in some part to any contact or pose based measurement robot. The test setup used for the experiments can also be used to track & quantify improvements in the design, as shown in section 5.2.

Another improvement to future measurement systems could come from exploiting the fact that measurement devices also have the capability of constructing structures. By constructing specific temporary structures, the deformations in the primary structure can be amplified. For the bending case an example deformation amplifying structure has been presented in Figure 8.1.

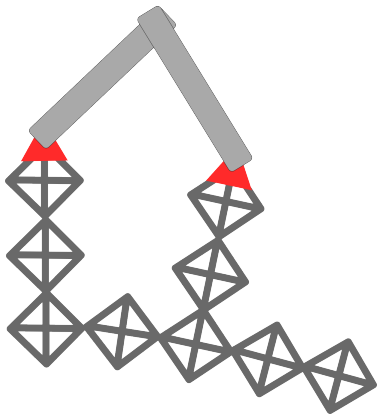

Figure 8.1: Temporary pillar structures constructed over the surface of a beam, allowing amplification of bending deformations.

While the current project covered only single robot measurements, future systems are expected to employ multiple robots for manufacturing. The multitude of robots can also be used to the advantage of the measurement system. One way of taking advantage of numerous robots is by providing more coverage of the structure with simultaneous independent measurements. Likewise, multiple robots can be used to collaboratively measure the structure with measurement schemes similar to strain gage chains used to measure strain gradients over a length or strain gage rosettes used to measure bidirectional strain in higher dimensional structures (2D surfaces or surface measurements on 3D solids as opposed to measurements of 1D beams).

To conclude, the implications of a complete structural system which is self-aware cannot be understated. During manufacturing, self-awareness not only allows the system to better account for physical changes occurring to the structure but also provides awareness of and robustness against unaccounted external disturbances. On the long term, during structure operation, the monitoring allows for monitoring of material & structural properties as well as operational conditions. Long-term monitoring could allow structures to be operated more safely by repairing the structure where lattice properties seem to have deteriorated. Long term monitoring also allows modifying the structure using in-situ optimization, where changes can be made to the geometry of the structure can reduce weight or increase stiffness. As such, the potential benefits of integrating measurement systems into the structural system make further research a rewarding endeavour.

Bibliography

[1] James Edward Gordon. *Structures: or why things don't fall down*. Da Capo Press, 2009.

[2] Benjamin Jenett et al. "Material–Robot System for Assembly of Discrete Cellular Structures". In: *IEEE Robotics and Automation Letters* 4.4 (July 2019), pp. 4019–4026. DOI: 10.1109/lra.2019.2930486.

[3] Alex Luijten. "Self-assembling ultra-lightweight lattice structures". MA thesis. ETH Zurich, 2020.

[4] Guillermo Presa Magriña. "Autonomous assembly of digital materials". MA thesis. Faculty of Aerospace Engineering: TU Delft, 2024. URL: https://resolver.tudelft.nl/uuid:9053ca77-cb4d-4da5-8b97-c29832167743.

[5] Tobias A. Schaedler et al. "Architected Cellular Materials". In: *Annual Review of Materials Research* (2016). DOI: 10.1146/annurev-matsci-070115-031624.

[6] Elisabetta Repossi. "On the mathematical modeling of a metal foam expansion process". PhD thesis. Politecnico di Milano, 2015. URL: https://hdl.handle.net/10589/108605.

[7] Michael F. Ashby. "The properties of foams and lattices." In: *Philosophical Transactions of the Royal Society A* 364.1838 (Jan. 2006), pp. 15–30. DOI: 10.1098/rsta.2005.1678.

[8] Michael F Ashby and Lorna J Gibson. "Cellular solids: structure and properties". In: *Press Syndicate of the University of Cambridge, Cambridge, UK* (1997), pp. 175–231.

[9] Kenneth C. Cheung et al. "Reversibly Assembled Cellular Composite Materials". In: *Science* 341.6151 (Sept. 2013). MAG ID: 2062010943, pp. 1219–1221. DOI: 10.1126/science.1240889.

[10] Benjamin Eric Jenett. "Discrete mechanical metamaterials". PhD thesis. Massachusetts Institute of Technology, 2020.

[11] Emilio Barchiesi et al. "Mechanical metamaterials: a state of the art:" in: *Mathematics and Mechanics of Solids* (2019). DOI: 10.1177/1081286517735695.

[12] Ying Liu et al. "Design of mechanical metamaterials for simultaneous vibration isolation and energy harvesting". In: *Applied Physics Letters* (2017). DOI: 10.1063/1.5008674.

[13] T. Lewis and W. L. Stone. "Biochemistry, Proteins Enzymes". In: *StatPearls*. Lewis, Theodore Stone, William L Study Guide Book Chapter Disclosure: Theodore Lewis declares no relevant financial relationships with ineligible companies. Disclosure: William Stone declares no relevant financial relationships with ineligible companies. NBK554481 [bookaccession]. Treasure Island (FL): StatPearls Publishing Copyright © 2024, StatPearls Publishing LLC., 2024.

[14] Tommaso Toffoli and Norman Margolus. "Programmable matter: concepts and realization". In: *Physica. D, Nonlinear phenomena* 47.1-2 (1991), pp. 263–272.

[15] Jean-Marie Lehn. "Supramolecular chemistry—scope and perspectives molecules, supermolecules, and molecular devices (Nobel Lecture)". In: *Angewandte Chemie International Edition in English* 27.1 (1988), pp. 89–112.

[16] Satoshi Murata et al. "A 3-D self-reconfigurable structure". In: 1 (May 1998). MAG ID: 2140355478, pp. 432–439. DOI: 10.1109/robot.1998.677012.

[17] Paul Levi et al. “Reconfigurable swarm robots produce self-assembling and self-repairing organisms”. In: *Robotics and Autonomous Systems* 62.10 (Oct. 2014), pp. 1371–1376. DOI: 10.1016/j.robot.2014.07.001.

[18] Lijun Mao et al. “Highly efficient synthesis of non-planar macrocycles possessing intriguing self-assembling behaviors and ethene/ethyne capture properties”. In: *Nature Communications* 11.1 (2020). ISSN: 2041-1723. DOI: 10.1038/s41467-020-19677-x.

[19] Benjamin Jenett et al. “Meso-scale digital materials: modular, reconfigurable, lattice-based structures”. In: *International Manufacturing Science and Engineering Conference*. Vol. 49903. American Society of Mechanical Engineers. 2016, V002T01A018. DOI: 10.1115/msec2016-8767.

[20] Amira Abdel-Rahman et al. “Self-replicating hierarchical modular robotic swarms”. In: *Communications Engineering* 1.1 (2022), p. 35.

[21] Miana Smith, Amira Abdel-Rahman, and Neil Gershenfeld. “Self-Reconfigurable Robots for Collaborative Discrete Lattice Assembly”. In: *2024 IEEE International Conference on Robotics and Automation (ICRA)*. 2024, pp. 3624–3631. DOI: 10.1109/ICRA57147.2024.10609866.

[22] Stephanie J. Woodman et al. “Deployable Cuboctahedrons for Adaptive Space Infrastructure”. In: *2024 IEEE 7th International Conference on Soft Robotics (RoboSoft)*. 2024, pp. 75–81. DOI: 10.1109/RoboSoft60065.2024.10521988.

[23] I.H.M.S. Nettersheim et al. “Engineered Living Composite Materials”. In: *Composites Science And Technology* (2024). DOI: 10.1016/j.compscitech.2024.110758.

[24] Allan Costa et al. “Algorithmic Approaches to Reconfigurable Assembly Systems”. In: *2019 IEEE Aerospace Conference*. 2019, pp. 1–8. DOI: 10.1109/AERO.2019.8741572.

[25] Andreas Bironf. “Design of cellular structures for robotic assembly”. MA thesis. TU Delft, 2022.

[26] Dominic Hart. *Robot team builds high-performance digital structure for NASA*. Jan. 2024. URL: https://www.nasa.gov/general/robot-team-builds-high-performance-digital-structure-for-nasa/.

[27] A.G. Anisimov, R.M. Groves, and C. Schoemaker. *Delft University of Technology AE4ASM108 Course Reader Experimental Techniques & Non-Destructive Testing*. 2021.

[28] Heather A. Wade, ed. *The ASQ metrology handbook*. eng. 3rd ed. OCLC: 1410604737. Milwaukee: ASQ Excellence, 2022. ISBN: 9781523155910.

[29] R. E. Kalman. “On the general theory of control systems”. In: *IFAC Proceedings Volumes*. 1st International IFAC Congress on Automatic and Remote Control, Moscow, USSR, 1960 1.1 (Aug. 1960), pp. 491–502. ISSN: 1474-6670. DOI: 10.1016/S1474-6670(17)70094-8. URL: https://www.sciencedirect.com/science/article/pii/S1474667017700948 (visited on 10/30/2024).

[30] Nicolas Kubail Kalousdian et al. “Learning robotic manipulation of natural materials with variable properties for construction tasks”. In: *IEEE Robotics and Automation Letters* 7.2 (2022), pp. 5749–5756.

[31] Roger M. Groves and Roger M. Groves. “3.12 Inspection and Monitoring of Composite Aircraft Structures”. In: (Jan. 2018), pp. 300–311. DOI: 10.1016/b978-0-12-803581-8.10340-6.

[32] Randa Almadhoun et al. “A survey on inspecting structures using robotic systems”. In: *International Journal of Advanced Robotic Systems* 13.6 (Nov. 2016), p. 172988141666366. DOI: 10.1177/1729881416663664.

[33] Yongding Tian et al. “Intelligent robotic systems for structural health monitoring: Applications and future trends”. In: *Automation in Construction* 139 (July 2022), pp. 104273–104273. DOI: 10.1016/j.autcon.2022.104273.

[34] Hung Manh La. “Automated Robotic Monitoring and Inspection of Steel Structures and Bridges”. In: *arXiv: Robotics* (May 2017). DOI: 10.1017/s0263574717000601.

[35] Mohammad R. Jahanshahi et al. “Reconfigurable swarm robots for structural health monitoring: a brief review”. In: *International Journal of Intelligent Robotics and Applications* 1.3 (June 2017), pp. 287–305. DOI: 10.1007/s41315-017-0024-8.

[36] Tianyao Chen et al. “An Elbow Exoskeleton for Upper Limb Rehabilitation With Series Elastic Actuator and Cable-Driven Differential”. In: *IEEE Transactions on Robotics* 35.6 (Aug. 2019), pp. 1464–1474. DOI: 10.1109/tro.2019.2930915.

[37] J Lunenburg et al. “Tech United Eindhoven Team Description 2011”. In: July 2011.

[38] Jerry Pratt et al. “Virtual model control of a bipedal walking robot”. In: *Proceedings of International Conference on Robotics and Automation* 1 (Apr. 1997), pp. 193–198. DOI: 10.1109/robot.1997.620037.

[39] Jerry Pratt et al. “Exploiting inherent robustness and natural dynamics in the control of bipedal walking robots”. In: (Jan. 2000).

[40] Gill A. Pratt et al. “Series elastic actuators”. In: *Proceedings 1995 IEEE/RSJ International Conference on Intelligent Robots and Systems. Human Robot Interaction and Cooperative Robots* 1 (Aug. 1995), pp. 399–406. DOI: 10.1109/iros.1995.525827.

[41] Michael Ruderman et al. “Modeling and Identification of Elastic Robot Joints With Hysteresis and Backlash”. In: *IEEE Transactions on Industrial Electronics* 56.10 (Feb. 2009), pp. 3840–3847. DOI: 10.1109/tie.2009.2015752.

[42] Jemin Hwangbo et al. “Cable-Driven Actuation for Highly Dynamic Robotic Systems”. In: *IEEE/RJS International Conference on Intelligent RObots and Systems* (Oct. 2018), pp. 8543–8550. DOI: 10.3929/ethz-b-000279306.

[43] O. A. Bauchau and J. I. Craig. “Euler-Bernoulli beam theory”. In: *Structural Analysis*. Ed. by O. A. Bauchau and J. I. Craig. Dordrecht: Springer Netherlands, 2009, pp. 173–221. ISBN: 978-90-481-2516-6. DOI: 10.1007/978-90-481-2516-6_5. URL: https://doi.org/10.1007/978-90-481-2516-6_5.

[44] Howard W Johnson. *High-speed Digital Design, A handbook of Black Magic*. 1993.

[45] Eric Bogatin. *Bogatin’s practical guide to prototype breadboard and PCB design*. Electronic Book. 2021. URL: https://stanford-artech-patron.eb20.com/AccessTitle/ISBN/9781630818487.


TU Delft
Delft
University of
Technology


TU Delft
Delft
University of
Technology

Appendices


TU Delft
Delft
University of
Technology

A

Statement on use of AI tools

During the preparation of this work, I used LanguageTool[1] to spellcheck. I also made use of EndNote 20[2] and research rabbit[3] for reference management and visualization of citations, respectively (I am not certain if they use AI). After using these tools/services, I reviewed the outcome and I take full responsibility for the content of this work.

[1] https://languagetool.org/
[2] https://endnote.com/
[3] https://www.researchrabbitapp.com/


TU Delft
Delft
University of
Technology

B

Alternative Moment of Area Model

If the beam was not modelled as a bulk cellular material, the lattice geometry would play an important role in determining the moment of area I. Although not used in the main thesis, inspecting ”under the hood” of the geometry abstraction provides insight into the behaviour of the beam under bending.

The cross section varies along the lattice and so does the area moment of inertia. To calculate the moment of area one half of the lattice is considered, since the other half will just have the same solution but mirrored. The lattice half is divided into two segments, one segment with 4 beams' cross-sections moving outwards and a constant section with 4 other beams. Figure B.1 shows examples of the two cross-section regimes.

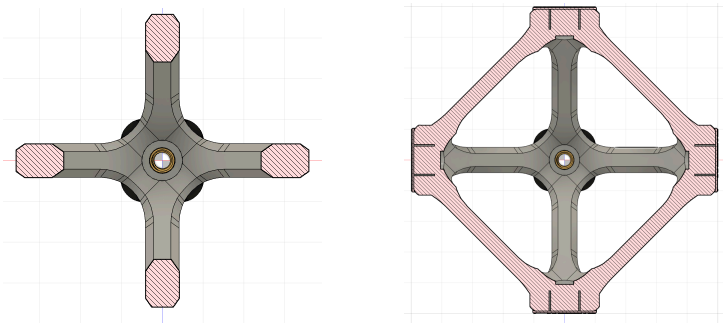

(a) The first segment with varying cross section.

(b) The second segment with constant cross section.

Figure B.1: Comparison of the two segments with varying and constant cross sections.

With the beam sections simplified to be of square cross sections instead of the bevelled square hexagons the moment of inertia along the lattice half can be calculated using the second moment of area relationship in Equation B.1. A plot showing the moment of inertia of cross-sections through the length of the (half) lattice is provided in Figure B.2. The figure shows that most bending deformations within the lattice will occur close to the attachment points, with the central section being geometrically stiffer.

$$I = \int y^2 dA, \tag{B.1}$$

where y is the vertical distance from the neutral axis passing through the center of the lattice.

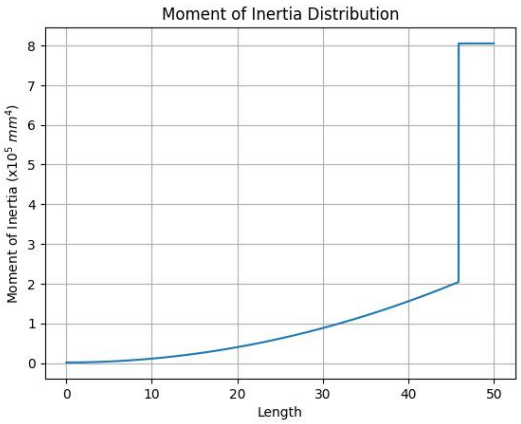

Figure B.2: Second moment of area for each cross section of the lattice half.

Using the parallel axis theorem shown in Equation B.2, the moment of inertia of 2x2 and 3x3 beams can also be found.

$$I_{\mathrm{YZ}} = I_{\mathrm{yz}} + A \times d_y, \tag{B.2}$$

where YZ is the principal axis about which the moment of inertia is to be calculated, yz is the axis about which the moment of inertia is known, A is the cross sectional area and d_y is the offset between the two axes.

In general most of the strain is expected to occur in the connection points where moment of inertia is lowest, causing the bending of the beam to occur almost discretely for each lattice traversed in the length direction.

C

Main PCB Power Circuit Re-design

The main printed circuit board for the ILLAv3 is a hub connecting the power source (batteries), servos, the x-bee wireless communications unit, and optionally an Arduino Uno unit. It features a step-down switching power converter to go from the 12V (or less depending on charge state) battery source to 3.3V, the operating voltage for the x-bee communications module. [4]

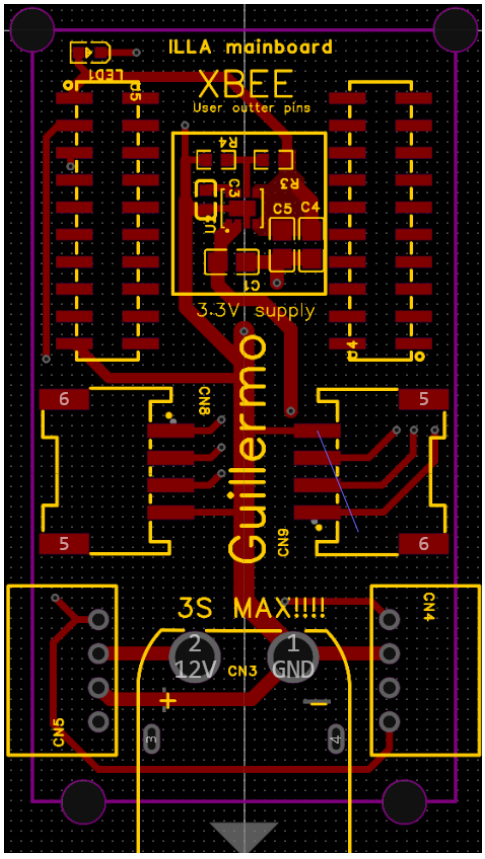

(a) ECAD drawing of the topside traces of the old ”main” printed circuit board.

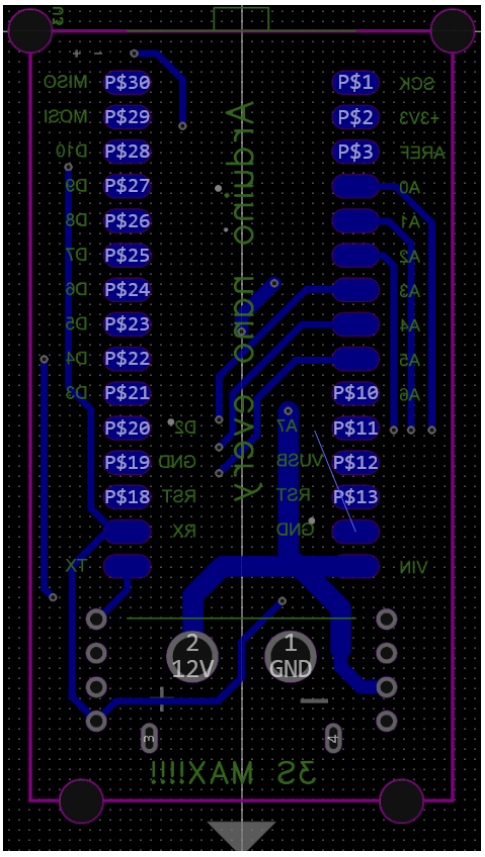

(b) ECAD drawing of the bottom side traces of the old ”main” printed circuit board.

Figure C.1: ECAD drawings of the old ”main” printed circuit board.

The previous design ran into issues with capacitor C1 in the power converter circuit blowing up when the board is connected as shown in Figure C.2.

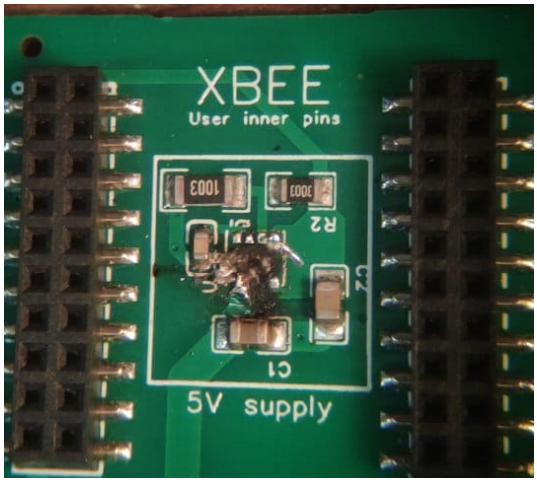

Figure C.2: Photo showing capacitor C1 after plugging the board in.

To improve the power distribution of the ”main” board, it has been re-designed with a more reliable switching converter circuit and improvements to the layup targeting improved power delivery and ground referencing. Figure C.4 shows the new and improved circuit diagram using a higher fidelity texas instruments switching power conversion chip and integrating test points which along with the 0 ohm resistors facilitate swapping of the circuit if the need arises and allow for easier inspection of the circuit.

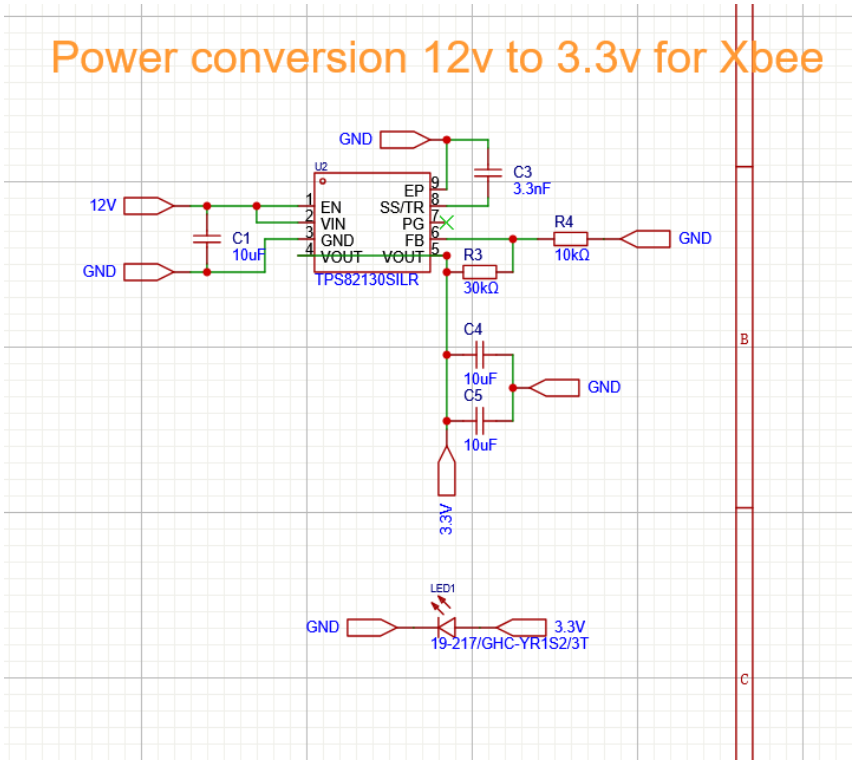

Figure C.3: Circuit diagram showing the power conversion circuit for the old ”main” printed circuit board.

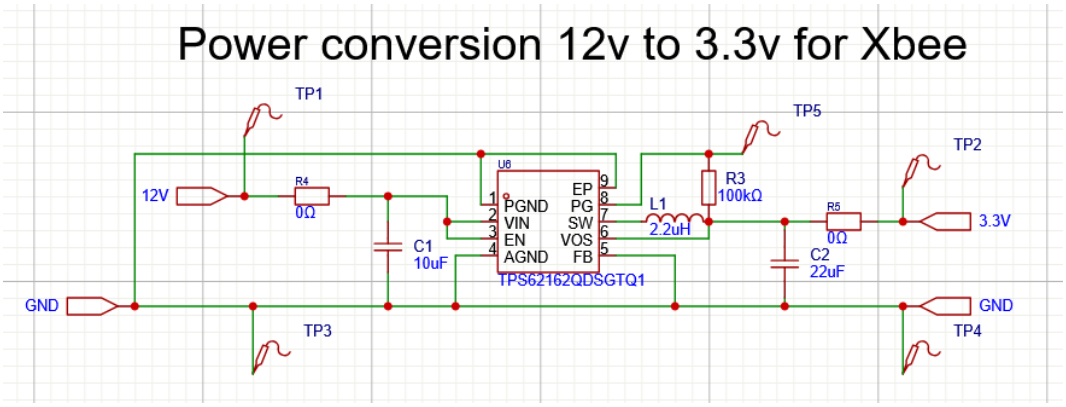

Figure C.4: Circuit diagram showing the power conversion circuit for the new ”main” printed circuit board.

As seen in Figure C.5a the packaging the circuit components, in particular the inductor L1 and capacitor C1 have been made larger. Additionally, both the topside and the bottom side seen on Figure C.5b now feature copper ground pours providing a closer ground reference to signals travelling and helping with the dissipation of heat from components.

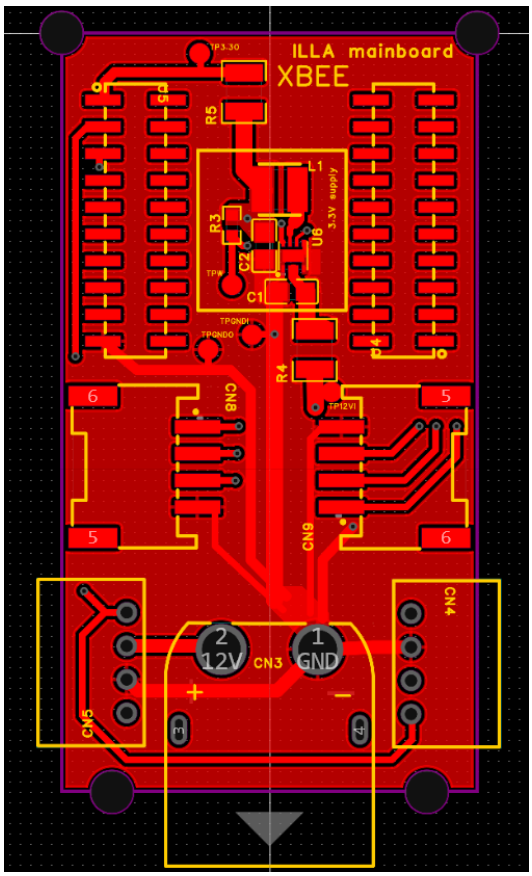

(a) ECAD drawing of the top side traces of the new ”main” printed circuit board.

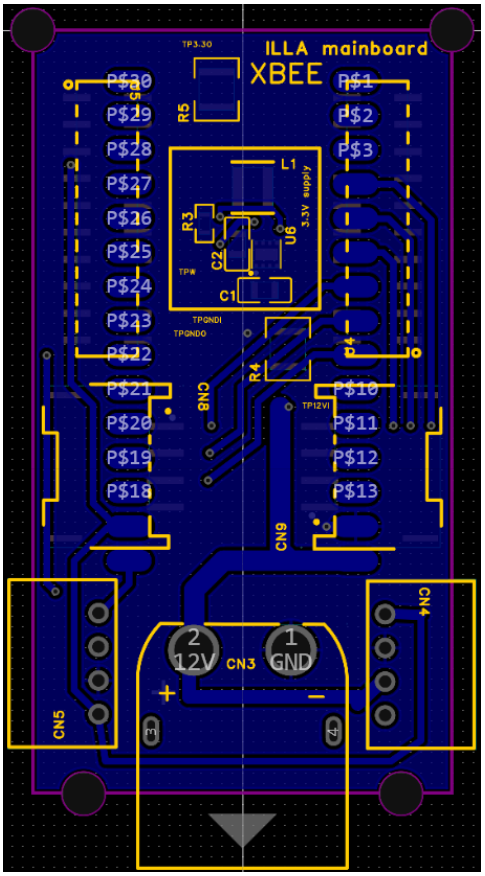

(b) ECAD drawing of the bottom side traces of the new ”main” printed circuit board.

Figure C.5: ECAD drawings of the traces of the new ”main” printed circuit board.

The board design has been improved following the advice of Phil Salmony as well as tips from the books High-Speed Digital Design: A Handbook of Black Magic [44] and Bogatin’s practical guide to prototype breadboard and PCB design [45].